Geochemistry, Geophysics, Geosystems®

AGU ADVANCING EARTH AND SPACE SCIENCE

RESEARCH ARTICLE
10.1029/2021GC010208

Special Section:
Insights into Subduction Zone Processes from Models and Observations of Exhumed Terranes

Embrittlement Within Viscous Shear Zones Across the Base of the Subduction Thrust Seismogenic Zone

C. J. Tulley[1], Å. Fagereng[1], K. Ujiie[2], J. F. A. Diener[3], and C. Harris[3]

[1]School of Earth and Environmental Sciences, Cardiff University, Cardiff, UK, [2]Faculty of Life and Environmental Sciences, University of Tsukuba, Tsukuba, Japan, [3]Department of Geological Sciences, University of Cape Town, Cape Town, South Africa

Key Points:

- Brittle fracturing occurred locally within viscously deforming hydrated oceanic crust and subducted sediments
- Fracturing is localized at viscosity contrasts and *P-T* conditions of metamorphic dehydration reactions
- Rocks that deformed at *P-T* conditions away from dehydration reactions record dominantly viscous behavior

Supporting Information:

Supporting Information may be found in the online version of this article.

Correspondence to:
C. J. Tulley,
tulleycj@gmail.com

Citation:
Tulley, C. J., Fagereng, Å., Ujiie, K., Diener, J. F. A., & Harris, C. (2022). Embrittlement within viscous shear zones across the base of the subduction thrust seismogenic zone. *Geochemistry, Geophysics, Geosystems*, *23*, e2021GC010208. https://doi.org/10.1029/2021GC010208

Received 13 OCT 2021
Accepted 27 MAY 2022

Abstract Geophysical observations indicate that patches of localized fracturing occur within otherwise viscous regions of subduction plate boundaries. These observations place uncertainty on the possible down-dip extent of the seismogenic zone, and as a result the maximum magnitude of subduction thrust earthquakes. However, the processes controlling where and how localized fracturing occurs within otherwise viscous shear zones are unclear. We examined three exposures of exhumed plate boundary on Kyushu, Japan, which contain subducted sediments and hydrated oceanic crust deformed at ~300 to ~500°C. These exposures preserve subduction-related viscous deformation, which in two of the studied exposures has a mutually overprinting relationship with quartz veins, indicating localized cyclical embrittlement. Where observed, fractures are commonly near lithological contacts that form viscosity contrasts. Mineral equilibrium calculations for a metabasalt composition indicate that exposures showing cyclical embrittlement deformed at pressure-temperature conditions near dehydration reactions that consume prehnite and chlorite. In contrast, dominantly viscous deformation occurred at intervening pressure-temperature conditions. We infer that at conditions close to metamorphic dehydration reactions, only small stress perturbations are required for transient embrittlement, driven by localized dehydration reactions reducing effective stress, and/or locally increased shear stresses along rheological contrasts. Our results show that the protolith composition of the subducting oceanic lithosphere controls the locations and magnitudes of dehydration reactions, and the viscosity of metamorphosed oceanic crust. Therefore, compositional variations might drive substantial variations in slip style.

Plain Language Summary Along tectonic plate boundaries, with increasing depth, pressure and temperature, plate movement by brittle fracturing is suppressed, and mechanisms allowing steady slip become more efficient. Along subduction plate boundaries, where one plate sinks beneath another, observations indicate that a proportion of slip sometimes occurs by fracturing at pressure-temperature conditions where steady slip typically dominates. We use outcrops of an ancient, inactive plate boundary exposed on Kyushu, Japan to investigate the reason for this behavior. We found that chemical reactions, triggered by increasing temperature in sinking oceanic crust, produce water, with the effect of locally raising the fluid pressure within the plate boundary. We suggest that locally raised fluid pressures assist fracturing at pressure-temperature conditions where steady slip typically dominates. In some outcrops, fractures are especially common along contacts between different rock types, suggesting that mixing of different materials along the plate boundary might also favor fracturing.

1. Introduction

Earthquakes typically nucleate within a depth range referred to as the seismogenic zone. The base of the seismogenic zone depends on temperature (*T*), pressure (*P*) and composition, and in subduction zones a transition to dominantly aseismic creep typically occurs at ~350°C or the upper plate Moho, whichever is shallower (Hyndman et al., 1997). The transition zone between seismogenic and aseismic depths may span several km down-dip along the plate boundary, and is home to a range of intermediate slip styles (e.g., Obara & Kato, 2016; Peng & Gomberg, 2010). These include episodic tremor (persistent low frequency seismic signals consistent with small brittle slip events; Ide et al., 2007; Obara, 2002) and slow slip events (slip of similar magnitude to earthquakes but too slow to radiate seismic energy) (Peng & Gomberg, 2010; Rogers, 2003). The potential for earthquake propagation in this transition zone remains unclear (Obara & Kato, 2016). Understanding the factors

that control where and how intermediate slip styles arise is therefore important for estimating potential rupture areas and the associated range of earthquake magnitudes (e.g., Marone, 1998; Scholz, 1998).

Along subduction plate boundaries, localized embrittlement within otherwise aseismic regions may be triggered by either or a combination of locally reduced effective stresses (e.g., Fagereng, Diener, Meneghini, et al., 2018; Gao & Wang, 2017; Giuntoli & Viola, 2021; Shelly et al., 2006; Yardley, 1983), or locally increased shear stress (Beall et al., 2019a; Sibson, 1980). Direct constraints on the composition and internal geometry of plate boundary shear zones may provide insight into how and why variations in shear stress or effective stress occur. Exposures of exhumed plate boundaries preserve structures that developed progressively during plate boundary slip, and if later tectonic or metamorphic overprint can be avoided, such exposures provide opportunities to directly observe the time-integrated effects of plate boundary deformation, and potentially constrain these factors.

Subducted and metamorphosed sedimentary rocks and oceanic crust are exposed on Kyushu, Japan, and some exposures preserve structures and mineral assemblages developed during subduction along the Late Cretaceous Eurasian margin. We consider three exposures of the Late Cretaceous plate boundary on Kyushu that were exhumed from different *P-T* conditions, and show minor post-subduction overprint. The metamorphic grades preserved in the studied exposures transect the inferred thermally-controlled seismic-aseismic transition (~350°C; Brace & Kohlstedt, 1980; Hyndman et al., 1997) and give a depth-integrated geological view of the plate boundary shear zone below the 300°C isotherm, extending to ~500°C near the mantle-wedge corner. Outcrop *P-T* constraints suggest the exposures reflect a plate boundary with a relatively warm paleo-geotherm (~>15°C/km), and the temperature range of the exposures contains the temperatures at source regions for episodic tremor and slow slip (ETS) phenomena along the relatively warm Cascadia (McCrory et al., 2014; Wech & Creager, 2011) and southwest Japan margins (Obara et al., 2010; Obara & Kato, 2016).

In some of the shear zone exposures, viscously-formed foliations and brittlely-formed quartz veins mutually overprint, suggesting cyclicity in deformation style, as also suggested for many other exhumed shear zones (e.g., Behr & Bürgmann, 2021; Compton et al., 2017; Fagereng, Diener, Meneghini, et al., 2018; Fisher et al., 1995; Kirkpatrick et al., 2021; Kotowski & Behr, 2019; Meneghini & Moore, 2007; Rowe et al., 2011). Progressive metamorphism of subducting oceanic lithosphere is expected to produce different mineral assemblages depending on the input sequence and *P-T* path, which may sequester and/or release metamorphic fluids at different *P-T* conditions. Spatial variations in the mineral assemblage and fluid pressure within the shear zone may affect the mechanical conditions within the shear zone, and cause km-scale variations in deformation style (e.g., Condit et al., 2020; Fagereng, Diener, Ellis, & Remitti, 2018; Peacock, 2009).

We conceptualize and quantify mechanical conditions along the plate boundary using a combination of structural observations at outcrop- (100's m to cm) and thin section- (cm to μm) scale, supplemented by calculations of mineral equilibria in *P-T* space, and O isotope analysis to determine the provenance of vein-forming fluids. Our results allow us to address the following questions: (a) What are the physical processes responsible for brittle and viscous deformation within the plate interface? (b) Is there a relationship between the *P-T* conditions of metamorphic dehydration reactions and the *P-T* conditions of embrittlement? (c) Is localized embrittlement correlated with viscosity heterogeneity? (d) What controls the spatial distribution of embrittlement within the dominantly aseismic regime?

2. Tectonic Setting for the Exhumed Shear Zones

The geology of Kyushu is dominated by approximately northeast–southwest striking terranes comprising oceanic lithosphere and trench-fill sediments (Figure 1a; Wallis et al., 2020). These terranes experienced subduction followed by accretion along the eastern Eurasian margin during a history of dominantly convergent tectonics, beginning in the Cambrian (Wallis et al., 2020).

The Makimine mélange is exposed in eastern to central Kyushu, and occurs within the Late Cretaceous Shimanto Accretionary Complex (Figure 1a; Hara & Kimura, 2008; Kimura, 1997; Taira et al., 1982). In eastern Kyushu the Makimine mélange is exposed in outcrops that span a few tens of meters wide and continue for hundreds of meters along the coast (Figure 1c; Ujiie et al., 2018). In central Kyushu the Makimine mélange is exposed along river beds, in outcrops a few tens of meters wide, largely continuous for hundreds of meters along-river. In both coastal and inland mélange exposures, outcrops show sea-floor and trench-fill sediments, and oceanic crust

10.1029/2021GC010208

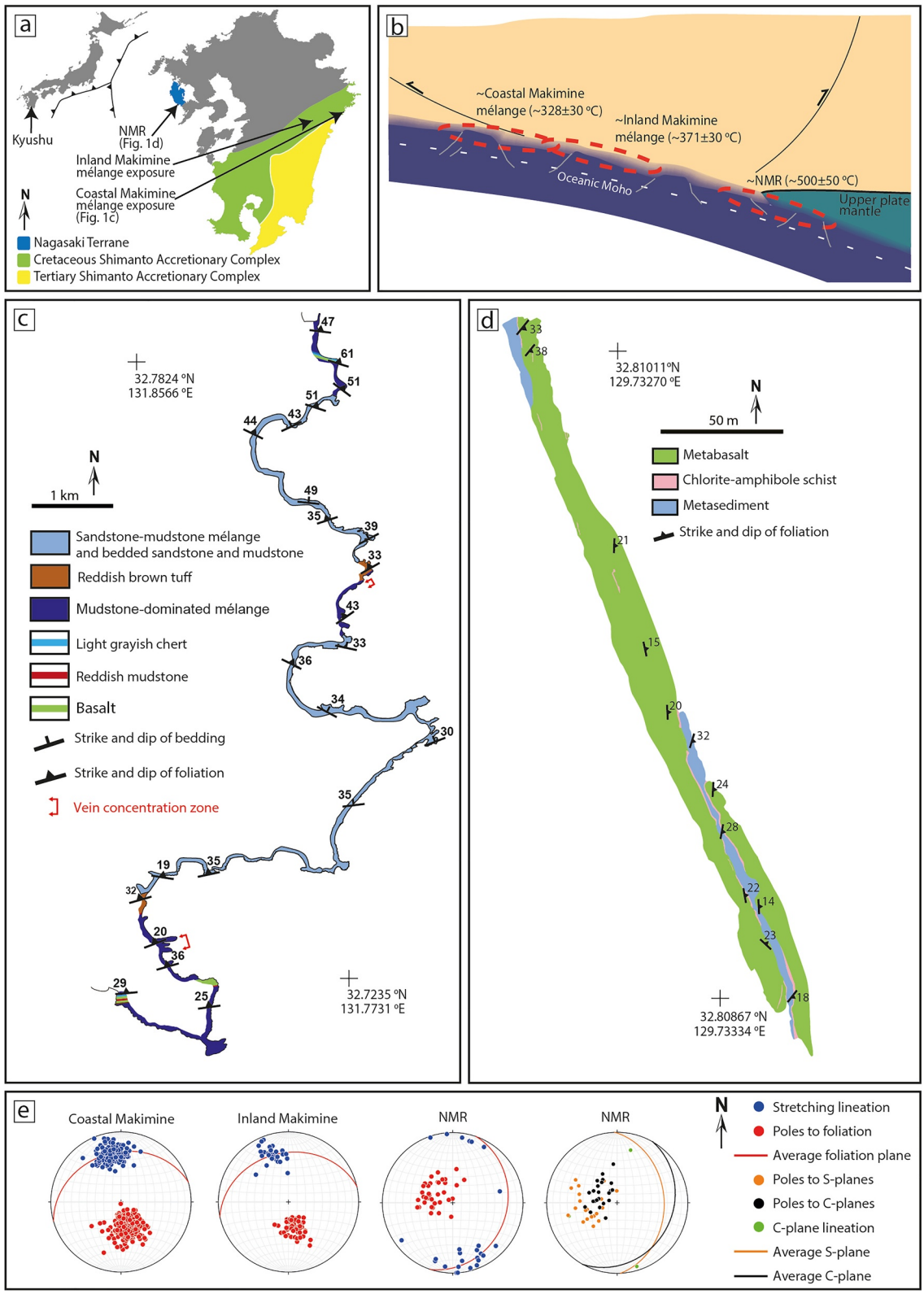

Figure 1.

metamorphosed and deformed at prehnite-pumpellyite to greenschist facies conditions, with a top-south shear sense (Mackenzie et al., 1987; Needham & Mackenzie, 1988; Ujiie et al., 2018). Peak temperature estimates derived from Raman spectra of carbonaceous material (RSCM) suggest that carbonaceous material defining the foliation in coastal (eastern) mélange exposures experienced peak T 328 ± 30°C (Ujiie et al., 2018). RSCM thermometry of metasediment from inland (western) mélange exposures (approx. 32.6128°N, 131.4512°E) suggests peak T in the range 371 ± 19°C; slightly warmer than for coastal exposures (Ujiie et al., 2019).

On the west coast of Kyushu, west of the Makimine mélange, the Nishisonogi metamorphic rocks (NMR), which have a Late Cretaceous metamorphic age (Faure et al., 1988; Hattori & Shibata, 1982), occur within the Nagasaki Terrane (Figure 1a). Similarities in lithology, minerology, and protolith and metamorphic ages suggest the NMR may instead be affiliated to the Sanbagawa terrane (Miyazaki et al., 2016), however this correlation is debated (Wallis et al., 2020). The NMR contains components of an ocean floor sequence as well as serpentinite potentially sourced from the mantle wedge (T. Nishiyama, 1989). At Nishikashiyama (Figure 1d) there is no intact ocean plate stratigraphy preserved; rather, components of an ocean floor sequence including schistose metabasalts and metasediments, are intermixed in exposures of a broad kilometer-scale shear zone. RSCM thermometry of metasediment from Nishikashiyama suggests peak metamorphism at 500 ± 50°C (Ujiie et al., 2019). This is consistent with regional temperature estimates (Mori et al., 2019) and the occurrence of hornblende in metabasalt, as psuedosections of metabasalt compositions (Figure 7a) indicate hornblende is the stable amphibole above ~475°C.

At Nishikashiyama, foliation dips gently east and lineation plunges gently south-southeast, features interpreted to be affected by a kilometer-scale, upright, open antiform with a north–south striking hinge surface west of Nishikashiyama (see Mori et al., 2019, their Figure 1b). This fold is interpreted to post-date the peak prograde metamorphism (Faure et al., 1988; T. Nishiyama, Sumino, & Ujiie, 2020). Unfolding by restoring the foliation to horizontal, S-C foliation geometries and lineation on C planes retain a top-south shear sense consistent with northwards subduction (Tulley et al., 2020). At Yukinoura, ~13 km northwest from the studied exposures (see T. Nishiyama, Ohfuji, et al., 2020, their Figure 1c), microdiamonds in metasediment, and garnet-bearing metabasalts with possible pseudomorphs after lawsonite, suggest metamorphism at $P > 2.8$ GPa, before retrogression to amphibolite facies equilibria (T. Nishiyama, Sumino, & Ujiie, 2020). The exhumation mechanism for the very high-pressure indicators is not clear. In contrast to exposures at Yukinoura, the exposures at Nishikashiyama do not preserve signs of retrogression from such high pressures.

Tectonic reconstructions indicate that in the Late Cretaceous, young to moderately aged ($\sim<$ 60 Ma) oceanic lithosphere subducted northwards along the northeast–southwest striking Eurasian margin (Muller et al., 2008; Whittaker et al., 2007). Northwards subduction along a northeast–southwest striking margin is consistent with the top-south shear inferred for the Makimine mélange and the NMR. On this basis, we interpret the Makimine mélange and NMR to have deformed along a similar, northeast–southwest striking plate boundary, accommodating subduction of young to moderately aged, relatively warm oceanic lithosphere.

3. Methods

We examined outcrop-scale structures such as foliations and quartz veins within metamorphosed and deformed sediments and oceanic crust in three exposures of exhumed shear zones on Kyushu, SW Japan. Samples obtained from the outcrops were analyzed using a combination of optical and electron microscopy to determine minerology and microstructure. Electron microscope work used the Zeiss Sigma HD scanning electron microscope in the School of Earth and Environmental Sciences, Cardiff University, equipped with two Oxford Instruments 150 mm^2 energy-dispersive spectrometers (EDS) and an Oxford Instruments electron backscatter diffraction (EBSD) detector. Electron backscatter diffraction data, used to quantify quartz microstructures, were processed using the MTEX toolbox for MATLAB (Bachmann et al., 2010).

Figure 1. Location and geological maps of the studied shear zones on Kyushu (coordinates; WGS84), and inferred setting prior to exhumation. (a) Tectonic setting of Kyushu, showing the location of the studied exposures. (b) Schematic cross section showing the inferred setting of the exhumed shear zones. (c) Geological map of coastal Makimine mélange (modified from Ujiie et al., 2018). (d) Geological map of the Nishisonogi metamorphic rocks at Nishikashiyama. (e) Stereoplots showing the orientations of lineations and poles to foliations for each of the studied localities, and S-C foliation geometries measured at Nishikashiyama. Average planes were computed using all data-points.

Quartz veins were sampled for O isotope analyses to constrain the source of the vein-forming fluids. We sampled veins that cross-cut foliations defined by the peak metamorphic assemblage, but are also viscously deformed with subduction-related kinematics. Analyses of quartz vein $\delta^{18}O$ were made at the University of Cape Town following the laser fluorination method of Harris and Vogeli (2010). 2–3 mg of clean quartz chips were reacted with BrF_5 and collected as O_2. The $^{18}O/^{16}O$ ratio of the O_2 gas was measured with a Finnegan Mat DeltaXP mass spectrometer in the Department of Archeology. Raw data were converted to δ-notation relative to standard mean ocean water based on an internal garnet standard (MON GT; $\delta^{18}O = 5.38‰$). Long-term variations in the measured $\delta^{18}O$ of standards indicate $2\sigma = 0.15‰$.

To improve estimates of the *P-T* conditions of deformation, and estimate amounts and conditions of fluid release in *P-T* space, mineral equilibrium calculations were conducted for a metabasalt composition from inland Makimine mélange (Table S1 in Supporting Information S1). Calculations were completed in the Na_2O-CaO-K_2O-FeO-MgO-Al_2O_3-SiO_2-H_2O-TiO_2-O (NCKFMASHTO) chemical system using THERMOCALC version 3.45, and an updated version of the Holland and Powell (2011) thermodynamic data set 6.2 (6 February 2012). Calculations used the activity-composition relationships of Green et al. (2016), apart from the relations for prehnite and pumpellyite, which are from Holland and Powell (2011). Calculations below 350°C used a simplified version of the amphibole model that only considered Fe-Mg substitution in ideal actinolite. Additionally, at $T < 350$°C, K in the bulk composition was disregarded as biotite was the only stable K-bearing mineral. The analyzed metabasalt composition was converted to the ideal chemical system by disregarding minor amounts of Cr and Mn that cannot currently be accounted for in the activity-composition relations. C in the bulk composition relates to minor calcite within viscously deformed veins, and was also excluded from the calculations. However, in order to account for Ca in calcite, the stoichiometric amount of Ca required to form calcite from the available C was subtracted from the total Ca. Similarly, minor amounts of phosphorus (hosted in apatite) were not considered in the calculations, and the stoichiometric amount of Ca required to form apatite was also subtracted from total Ca. 77.3 mol.% of total Fe was taken to be Fe^{2+}, in line with typical values for metamorphosed mafic rocks (Rebay et al., 2010). The sample was assumed to be saturated with H_2O at all conditions.

4. Results

4.1. Tectonic Fabrics in the Exhumed Shear Zones

In coastal exposures of the Makimine mélange, oceanic plate stratigraphy is generally preserved. Sedimentary textures are also preserved, and thus we use sedimentary rock names to describe the metasedimentary rocks in this location, as in previous studies (Ujiie et al., 2018). Layers of greenish metabasalt and reddish mudstone up to a few meters thick are overlain by reddish-brown tuff, also a few meters thick. This sequence is overlain by sandstone-mudstone mélange and coherent turbidites (Figure 1c) that form a layer 1.3–1.6 km thick. This stratigraphic sequence is repeated at least twice, perhaps by underplating (Ujiie et al., 2018). Foliation in the mélange strikes approximately east–west, and dips gently to the north (Figures 1c and 1e; Ujiie et al., 2018). Metabasalt layers occur subparallel to the foliation and stratigraphic layering (Figures 1c and 2a). We do not observe pinch-and swell of metabasalt layers, suggesting that the viscosity contrast between mudstone and metabasalt is low. Sandstone occurs as competent lenses within mudstone (Figure 2b), which have long axes subparallel to the foliation dip. Sandstone lenses commonly show a sigmoidal shape consistent with top-south shear. Foliation in the mudstone and metabasalt is locally cross-cut by quartz veins (Ujiie et al., 2018), some of which are deformed within meter-scale localized shear zones (Figure 2d).

Inland exposures of the Makimine mélange show mostly continuous, but variable-thickness (cm–m) layers of metabasalt and metasediments (Figure 2e). Coherent ocean plate stratigraphy is not preserved at the studied locality, but Needham and Mackenzie (1988) show repetition of metabasalt- and metasediment-rich sequences in Makimine mélange at the kilometer-scale in central Kyushu, interpreted to reflect underplating. Metabasalt layers within metasediment show long wavelength, low amplitude pinch-and-swell, suggesting that metabasalt was slightly more viscous than metasediment at the conditions of deformation. Foliation in metabasalt and metasediment dips gently north, and stretching lineation is subparallel to foliation dip, similar to coastal Makimine mélange (Figure 1e). Quartz veins occur, although here, in contrast to coastal exposures, veins do not cross-cut the foliation, but instead are viscously stretched subparallel to the foliation (Figure 2f).

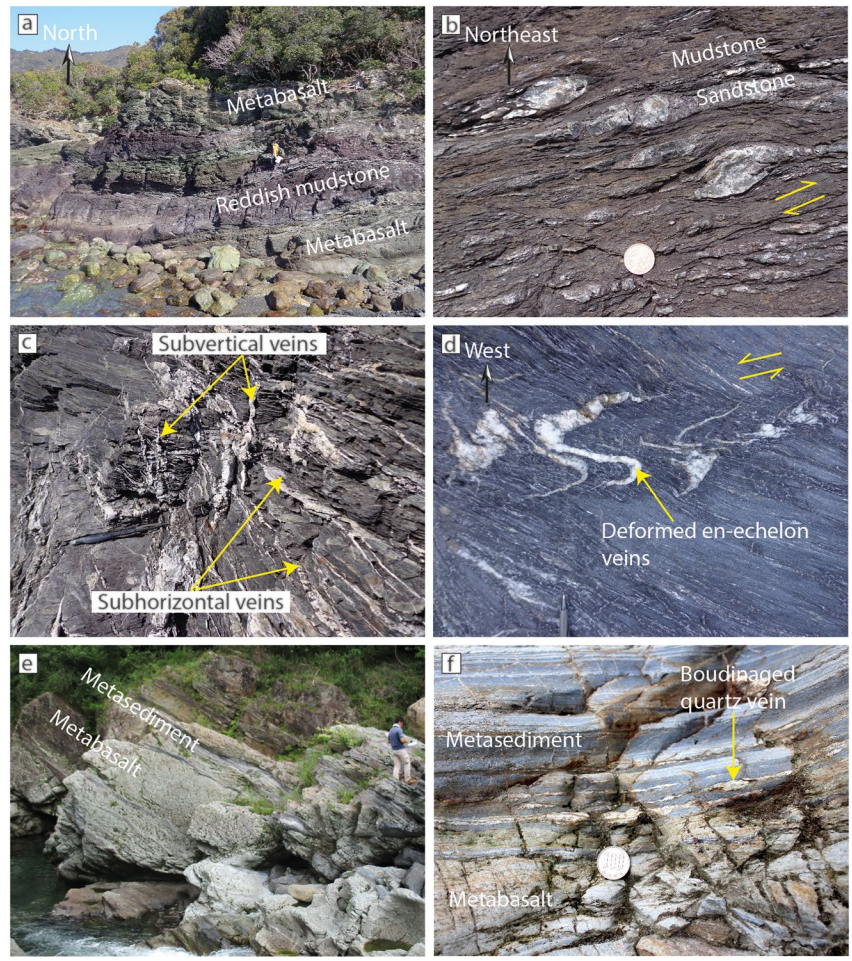

Figure 2. Structures from coastal (a–d) and inland (e–f) Makimine mélange: (a) Layers of greenish metabasalt and mudstone. (b) Sigmoidal lenses of quartzofeldspathic sandstone within mudstone, viewed approximately parallel to foliation dip. (c) Subvertical extension veins mutually cross-cut by subhorizontal veins. (d) En-echelon veins viscously deformed within a localized shear zone in mudstone. (e) Layers of greenish metabasalt with subtle pinch-and-swell structure, separated by metasediment. (f) Viscously deformed quartz veins subparallel to foliation.

At Nishikashiyama, the NMR contain layers of metasediment and metabasalt (Figure 1d) that vary in thickness from centimeters to several meters and lengths from meters to exceeding the extent of the outcrop (tens of meters). Foliation in metasediment and metabasalt generally dips east, but varies substantially in orientation at the cm to tens of meter scale because of tight, typically asymmetric folding commonly near lithological contacts (Figure 3a). Metasediment and metabasalt are commonly separated by centimeter-to-meter thick layers of chlorite-amphibole schist which has a more intense schistose texture and smaller proportion of albite, compared to metabasalt (Figures 3c–3f). Quartz veins occur both subparallel to the foliation and cross-cutting it at oblique angles, and show viscous deformation structures such as boudins and gentle to open folds (Figures 3c–3e).

4.2. Quartz Veins Within the Shear Zones

In coastal exposures of the Makimine mélange, shear veins occur subparallel to the mudstone cleavage (Figure 2c) and are identified by quartz slickenfibers on vein surfaces, and crack-seal textures indicating opening at low angles to vein boundaries. Inclusion bands defining the crack-seal texture within shear veins show spacing 20–38 μm (Ujiie et al., 2018). Extension veins, subparallel and oblique to the foliation (Figure 2c) are identified by vein-normal opening vectors; for example, quartz grains in extension veins are euhedral with long-axes orthogonal to the vein boundaries (Ujiie et al., 2018). Together the extension and shear veins form a pervasive fault-fracture mesh that accommodated a combination of dilation and top-south shear (Ujiie et al., 2018), as

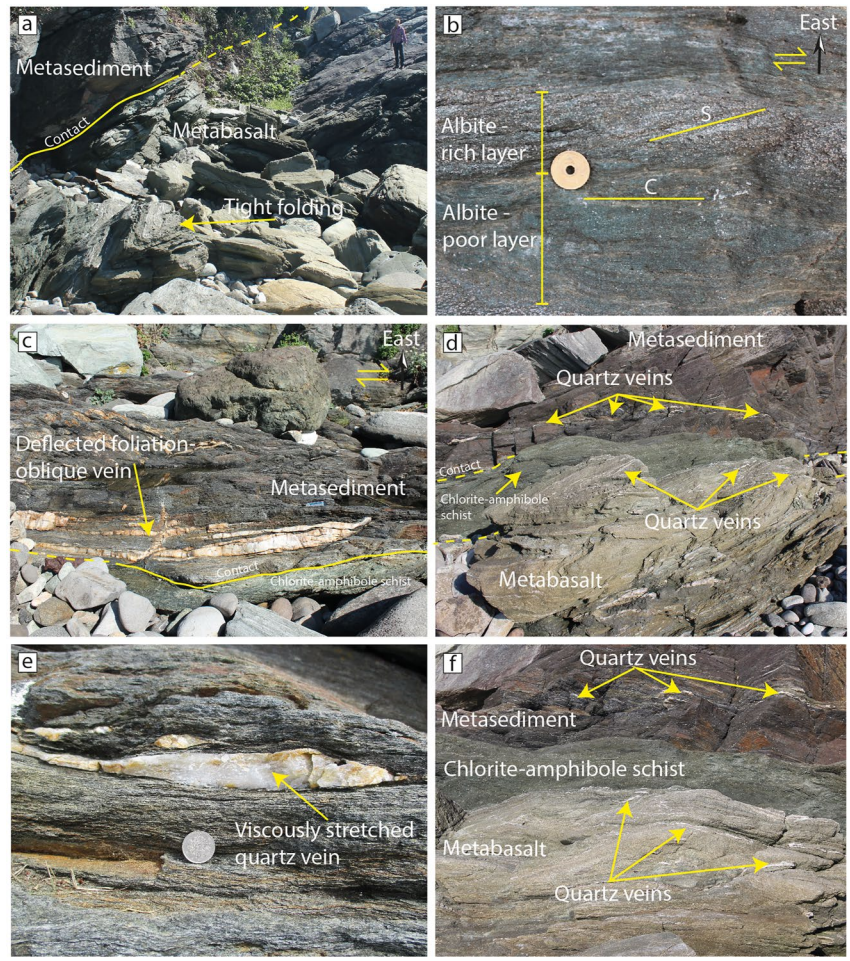

Figure 3. Structures within the Nishisonogi metamorphic rocks at Nishikashiyama, with inferred shear sense in (b) and (c) indicated by opposing arrows: (a) Tight folding in metabasalt near a contact with metasediment. (b) S-C foliation geometry within metabasalt consistent with top-south shear. (c) Foliation-parallel and foliation-oblique veins along a contact between chlorite-amphibole schist and metasediment, with local deflection of veins consistent with top-south shear. (d) Contact between metasediment and metabasalt separated by a ~ 1 m thick layer of chlorite-amphibole schist, showing locally abundant quartz veining. (e) Viscously stretched quartz vein within metasediment. (f) Abundant quartz veins near a contract between metasediment and metabasalt.

described for general cases by Sibson (1996) and Sibson (2017). The thickness of these veins varies from a few mm to ~5 cm, with typical lengths 1–2 m, although locally up to ~10 m. Areas of concentrated veining occur within the mudstone-dominated mélange unit (Figure 1c) and are inferred to be zones that experienced locally elevated strain rates (Ujiie et al., 2018). Some of the quartz veins have been viscously deformed within localized shear zones (Figure 2d).

Boudinage and pinch-and-swell geometries shown by veins in inland exposures of the Makimine mélange (Figure 2f) indicate viscous stretching within the plane of the foliation. Vein thicknesses vary between a few centimeters and a few hundred microns, and lengths range between micron-scale lenses interpreted as dismembered veins (Figure 5b), and examples up to ~2 m long that show pinch-and-swell structure. Unlike in coastal Makimine mélange, vein morphologies are less clear in outcrop (Figure 2f) and recrystallization related to viscous deformation has consistently overprinted growth-related structures such as fluid-inclusion planes or euhedral grains (Figure 5b).

In the NMR, veins occur subparallel and oblique to the foliation (Figure 3c). Like in inland Makimine mélange, veins subparallel to the foliation show pinch-and-swell and boudinage indicating viscous stretching. However, veins oblique to foliation show only small amounts of viscous overprint, such as deflections along foliation

planes (Figure 3c), that are consistent with top-south shear. These observations indicate that in the NMR fracture and vein precipitation was consistently followed by syn-subduction viscous deformation. The thickness of veins varies from a few mm to ~30 cm and veins range in length from ~1 m to at least 5 m, but the maximum traced length is limited by outcrop size. Qualitatively, near metabasalt-metasediment contacts the frequency of veins is especially high relative to the general frequency of veins in the study area (e.g., Figures 3d and 3f).

4.3. Microstructure of the Viscous Fabrics

In metabasalts from coastal Makimine mélange, albite-rich microlithons a few hundred microns thick, some of which show asymmetry consistent with top-south shear, are separated by layers rich in aligned chlorite grains (Figures 4a and 4b; Tulley et al., 2020). Minor proportions of prehnite occur, and prehnite grains are enveloped by the chlorite foliation (Figure 4b). Within metasediment, cleavage surfaces are defined by layers of fine-grained muscovite, which separate phyllosilicate-poor quartzofeldspathic layers (Figure 4d). The cleavage spacing is generally in the range 10–100 μm, with tighter spacing adjacent to quartz or albite grains that also

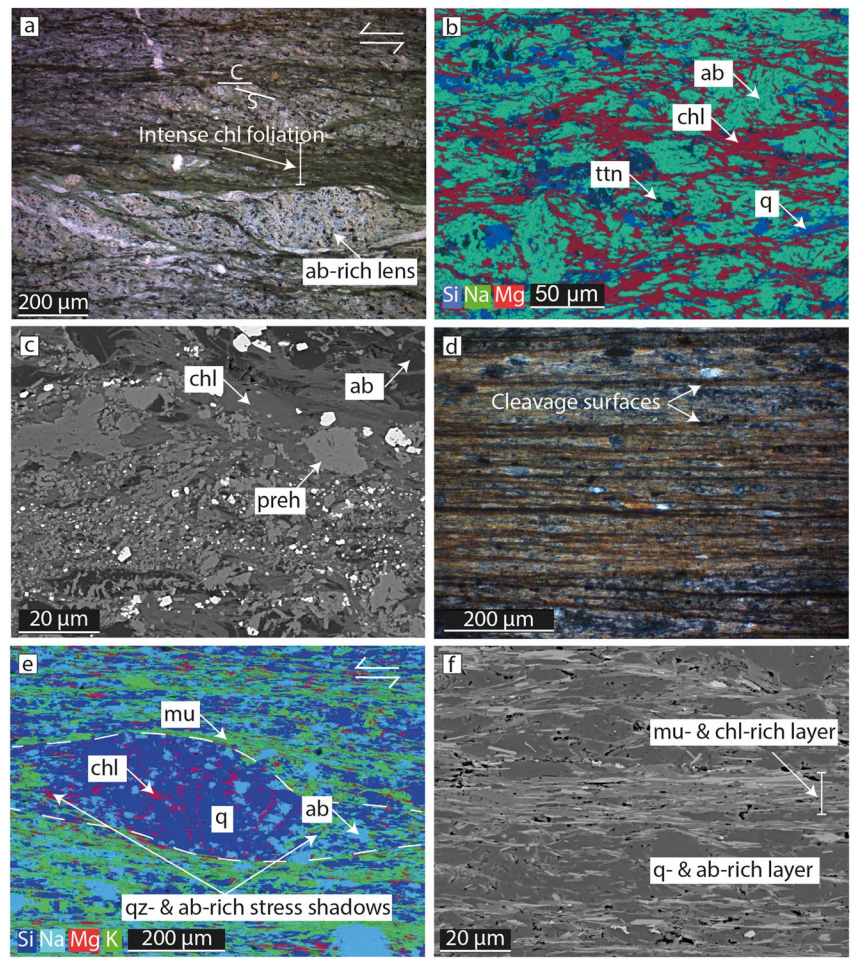

Figure 4. Microstructures of metabasalt (a–c) and metasediment (d–f) from coastal Makimine mélange. ab-albite; mu-muscovite; chl-chlorite; q-quartz; ttn-titanite; preh-prehnite. Opposing arrows in (a) and (e) indicate top-south shear. (a) Photomicrograph of metabasalt showing S-C structure. (b) Energy-dispersive spectrometers (EDS) map highlighting the distribution of chlorite around albite and quartz in metabasalt. (c) Backscattered electron image of metabasalt showing prehnite enclosed by the chlorite foliation. (d) Photomicrograph of metasediment showing the well-developed cleavage, with interstitial elongate quartz grains. (e) EDS map of metasediment, showing the muscovite-defined cleavage rotated adjacent to a quartz grain that shows asymmetry consistent with top-south shear. (f) Backscattered electron image showing the muscovite- and chlorite-rich layers that define the cleavage.

show asymmetry consistent with top-south shear (Figure 4e). Quartz and albite grains appear truncated against the cleavage and elongate parallel to the cleavage (Figure 4f).

In inland Makimine mélange, aligned muscovite and chlorite define the metabasalt foliation. Clinopyroxene, albite and amphibole form elongate grains that define the stretching lineation (Figure 5a). Mineral compositions obtained from EDS spectra indicate that clinopyroxene is diopside and amphibole is actinolite (Figure S1 in Supporting Information S1; Leake et al., 1997; Morimoto et al., 1988). Previously obtained EBSD data indicate a lack of subgrains in diopside, interpreted to reflect limited activity of dislocation creep (Tulley et al., 2020). Actinolite occurs in asymmetric stress shadows adjacent to diopside grains, and appears to have formed by the breakdown of diopside (Figure 5a). In metasediment, layers of muscovite define the foliation (Figure 5c), which is especially well developed adjacent to quartzite lenses, the long axes of which define the stretching lineation in metasediment (Figure 5b). Quartz veins and lenses consist of grains with undulose optical extinction and bulging boundaries, surrounded by smaller grains typically <10 μm with straighter optical extinction. Pole figures of average c-axis orientations for quartz grains in quartzite lenses show a well-developed crossed girdle geometry (Figure 5d). In contrast, average c-axis orientations for quartz grains within a quartz-rich area of the metasediment show a nearly random distribution (Figure 5d). Grain size measurements obtained from EBSD data suggest grain size 13 ± 7 μm (root mean square ± 1σ) within the quartz-rich area of the metasediment, and 18 ± 9 μm within viscously deformed veins (Figure 5d).

In NMR metabasalt, aligned elongate grains of albite and amphibole define the stretching lineation, and aligned muscovite and chlorite define the foliation, which commonly shows S-C geometry (Figures 3b and 6a; Tulley et al., 2020). Amphibole grains commonly show variation in composition, with more aluminous cores and less aluminous rims (Figure 6c). The geometry of the compositional zoning does not show any consistent anisotropy, and in many grains the zoning is fairly isometric. Mineral compositions obtained from EDS spectra, classified according to the scheme of Leake et al. (1997) indicate that amphibole compositions range between hornblende and actinolite, commonly with grain cores showing hornblende-like compositions and rims showing actinolite-like compositions (Figure S1 in Supporting Information S1). In NMR metasediment, muscovite defines the foliation, and the long axes of albite and quartz grains define the stretching lineation (Figure 6b). Garnet

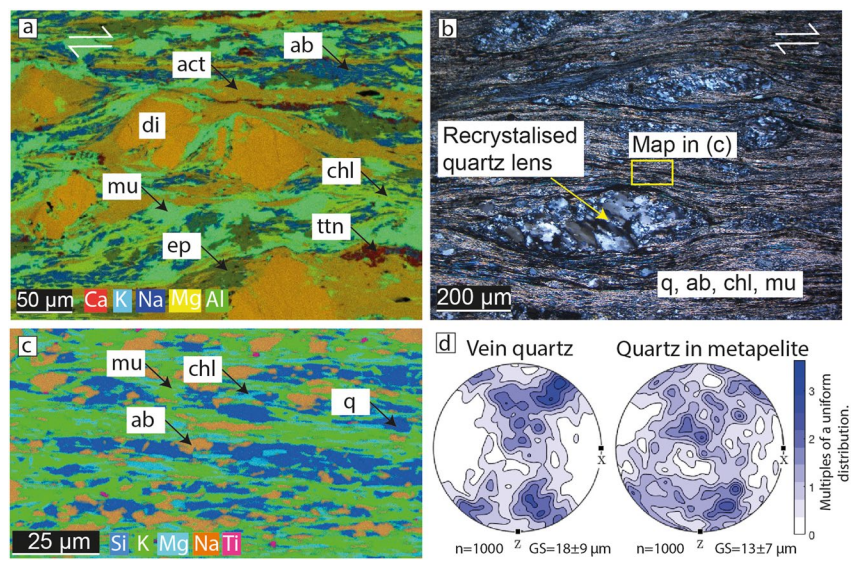

Figure 5. Microstructures of metabasalt (a) and metasediment (b and c) from inland Makimine mélange, and stereoplots showing quartz grain orientations in metasediment (d). Opposing arrows in (a and b) indicate top-south shear sense. di-diopside; act-actinolite; ep-epidote; other abbreviations as in Figure 4. (a) Energy-dispersive spectrometers (EDS) map showing the muscovite and chlorite-defined foliation wrapping diopside and albite grains. Actinolite occurs as asymmetric rims around diopside. (b) Photomicrograph of metasediment showing a sigmoidal lens of dynamically recrystallized quartz surrounded by intensely foliated metasediment. (c) EDS map showing segregated quartz-albite and chlorite-muscovite layers. (d) Equal area, lower hemisphere pole figures for average c-axis orientations of quartz grains in (left) a recrystallized vein, and (right) a quartz-rich region of the metasediment.

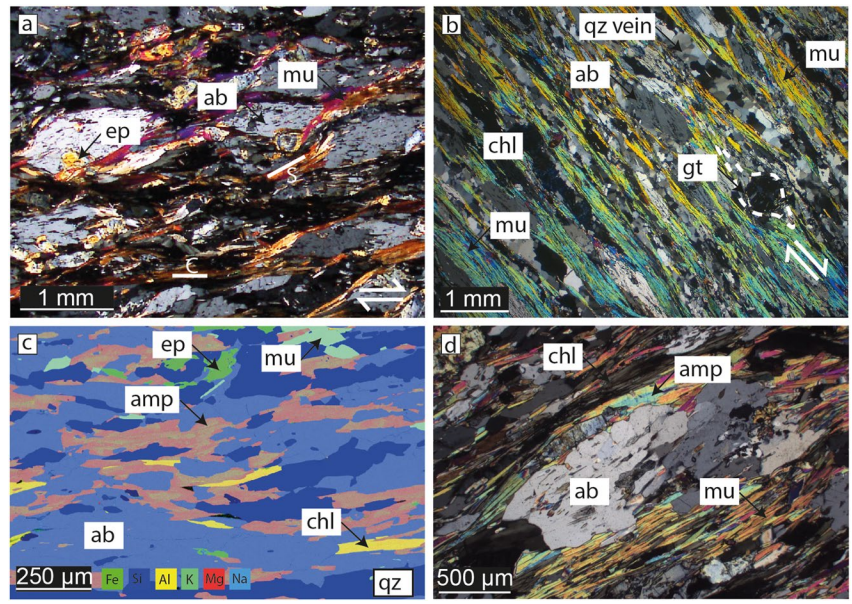

Figure 6. Microstructures of metabasalt and metasediment from the Nishisonogi metamorphic rocks. top-south shear sense indicated by opposing arrows. (a) Photomicrograph of metabasalt showing albite grains wrapped by muscovite, with S-C foliation geometry. (b) Photomicrograph of metasediment showing well-aligned muscovite separating layers of quartz and albite, and wrapping around garnet (gt). (c) Energy-dispersive spectrometers (EDS) map of metabasalt. Albite shows no chemical zoning, but amphibole (amp) shows approximately isometric zoning with a more aluminous composition in cores and a less aluminous composition in rims. (d) Photomicrograph of metabasalt, showing amphibole and the chlorite-muscovite foliation wrapping around albite.

occurs in small proportions (<5%). Quartz veins subparallel to the foliation in metabasalt and metasediment are characterized by low degrees of intragranular distortion and lobate grain boundaries.

4.4. Mineral Assemblages, Thermodynamic Equilibria and Metamorphic Dehydration Reactions

The metamorphic conditions of the studied shear zones suggest burial to far greater depths than the few kilometres where substantial fluid-bearing porosity is expected to be maintained (e.g., Saffer & Tobin, 2011), and the main source of fluids at the conditions of the exhumed shear zones is expected to be mineral-bound aqueous fluid released during metamorphic dehydration (Peacock, 1990). Therefore, fluid production depends on the mineralogy and hydration state of the subducting lithologies. In most cases, the oceanic crust will be volumetrically more significant than sediment (e.g., Peacock, 1990), and we therefore focus on fluid production from basalt protoliths.

Thermodynamically stable mineral assemblages calculated for an inland Makimine mélange metabasalt composition (Table S1 in Supporting Information S1), assuming water saturation, are shown in Figure 7a. At <0.6 GPa, and <260°C, the sample is calculated to consist of the typical prehnite-pumpellyite facies assemblage actinolite-chlorite-albite-prehnite-pumpellyite-quartz-titanite. With increasing temperature, a series of changes to the stable mineral assemblage occur over the narrow *T*-window 260–300°C, notably the loss of prehnite and pumpellyite in exchange for actinolite and epidote (Figures 7a and 7c). This series of changes represents a transition from the prehnite-pumpellyite facies to the greenschist facies. The broad *T* window 300–450°C, at <0.8 GPa, contains the typical greenschist facies assemblage actinolite-epidote-biotite- chlorite-albite-quartz-titantite (Figure 7a). Increasing *T* in the *P*-*T* region 450–475°C, 0.3–0.8 GPa, results in further mineralogical changes, notably the introduction and growth of hornblende at the expense of actinolite, epidote and chlorite (Figures 7a and 7d). These changes represent the transition from the greenschist facies to the amphibolite facies. In the high-*P*, low-*T* region of the diagram, lawsonite-blueschist facies equilibria appear at >0.9 GPa and <350–450°C. From within lawsonite-blueschist facies equilibria, increasing temperature results in the loss of Na-diopside and lawsonite, in exchange for actinolite and epidote. Overall, the topology of Figure 7a is similar to previous diagrams constructed for fresh and altered basalt compositions (e.g., Condit et al., 2020; Fagereng, Diener, Ellis, & Remitti, 2018; Fagereng, Diener, Meneghini, et al., 2018). As such, we anticipate that Figure 7, constructed for an inland

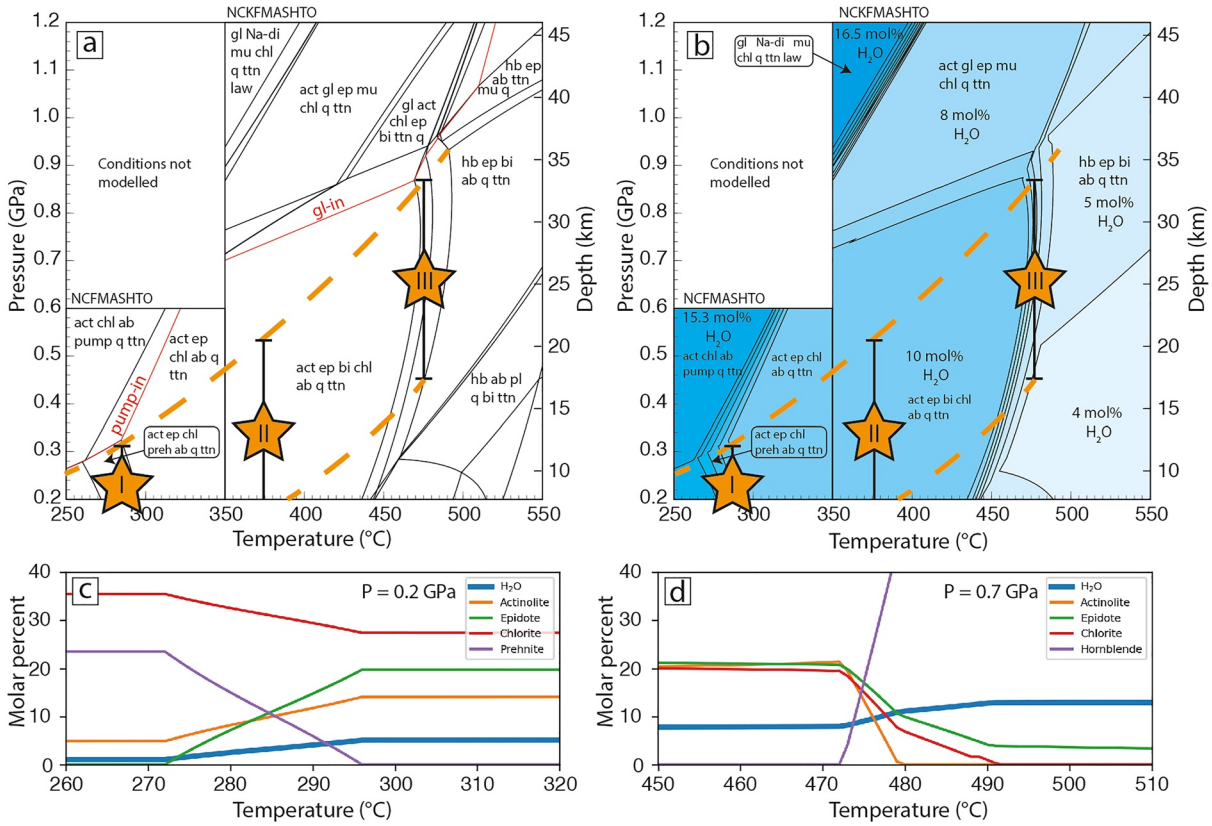

Figure 7. Thermodynamic constraints on shear zone *P-T* conditions, and *P-T* conditions of metamorphic dehydration reactions in oceanic crust. Dashed lines in (a and b) show the range of possible *P-T* paths for the studied Late Cretaceous margin. Orange stars indicate the inferred peak *P-T* conditions for (I) coastal Makimine mélange, (II) inland Makimine mélange and (III) Nishisonogi metamorphic rocks. For (I) and (III), *T* is constrained by sample mineralogy. RSCM thermometry constrains the *T*-condition for (II). Error bars show the possible *P*-range of the observed mineral assemblages. (a) Modeled mineral equilibria. (b) Contours for molar fractions of mineral-bound water. (c and d) show the evolution of the hydrous mineral assemblage and free water content near the peak *P-T* conditions of coastal Makimine mélange and the NMR, respectively. Abbreviations: chl = chlorite; ab = albite; pump = pumpellyite; preh = prehnite; q = quartz; ttn = titanite; ep = epidote; act = actinolite; bi = biotite; mu = muscovite; gl = glaucophane; hb = hornblende; pl = plagioclase; law = lawsonite; Na-di = Na diopside.

Makimine mélange composition, is a reasonable approximation for basalts from the other studied localities, which are interpreted to have formed along the same subduction margin albeit at different *P-T* conditions.

In coastal Makimine mélange, metabasalt contains albite, chlorite, epidote, quartz, titanite, magnetite and minor prehnite. This assemblage is consistent with the modeled equilibria at 260–290°C and <0.3 GPa (Figure 7a), with the exception that minor (<10vol.%) actinolite present in the modeled equilibria is not seen in thin section. Foliation-defining chlorite wraps around prehnite grains (Figure 4c), implying that prehnite was present during the final stages of subduction-related foliation development. Analcite, not observed in coastal Makimine metabasalts, is expected to become stable at <~0.2 GPa (Liou, 1971), suggesting the preserved mineral assemblage developed between 0.2 and 0.3 GPa, with the upper *P* limit constrained by the absence of pumpellyite (Figure 7a). The small difference between the peak *T* estimate from previous Raman analyses (328 ± 30°C; Ujiie et al., 2018), and the *T* constraint from Figure 7a (260–290°C) may be due to slight differences between the composition of coastal Makimine metabasalt and the modeled metabasalt composition from inland Makimine mélange, additional uncertainties in the Raman thermometry, or sluggish reaction rates during prograde metamorphism.

In inland Makimine mélange (peak *T* 371 ± 19°C; Ujiie et al., 2019), metabasalt contains albite, quartz, chlorite, muscovite, epidote, actinolite and diopside. EDS maps show that diopside is partially replaced by actinolite formed in asymmetric stress shadows (Figure 5a), implying progressive but partial equilibration of the metabasalt under hydrous conditions during viscous deformation. As diopside grains are rounded, fractured and rimmed by actinolite, they clearly predate the main metamorphic mineral assemblage. This, and the diopside composition, consistent with high-*T* low-*P* igneous rocks, suggests that diopside is a relict igneous mineral.

The lack of prehnite and hornblende in inland Makimine metabasalt is consistent with a peak metamorphic T in excess of the conditions of prehnite breakdown, occurring over the range 280–330°C, but below the actinolite-hornblende transition, occurring over the range 450–475°C. These constraints are consistent with the temperature estimate 371 ± 19°C obtained by Ujiie et al. (2019). Assuming a peak metamorphic temperature of 371 ± 19°C, the lack of glaucophane suggests inland Makimine mélange exposures experienced peak pressures <0.7 GPa (Figure 7a).

NMR metabasalt contains albite, amphibole, chlorite and epidote. The compositional zoning in some amphibole grains (Figure 6c and Figure S1 in Supporting Information S1) suggests that actinolite formed after hornblende. Anisotropic structures such as S-C foliation geometries and asymmetric albite grains suggest these features formed during shear, however compositional zoning in amphibole is fairly isotropic, consistent with having formed under largely static conditions, perhaps during exhumation. This interpretation is supported by Figures 7a and 7d that show hornblende is replaced by actinolite along a retrograde metamorphic path between 450 and 500°C and 0.2–1 GPa. Assuming peak thermal metamorphism at 500 ± 50°C (Ujiie et al., 2019), the lack of glaucophane in NMR metabasalt suggests peak pressures <1.1 GPa (Figure 7a).

In contrast to metabasalts, metasediments from the studied exposures show only minor mineralogical changes with increasing metamorphic grade. Coastal Makimine and inland Makimine mélange metasediments show the same mineral assemblage in similar proportions; quartz, albite, muscovite, and chlorite. NMR metasediments differ only slightly, due to the presence of minor amounts of garnet.

The constraints on peak P and T provided by metabasalt mineralogy, supported by RSCM thermometry (Mori et al., 2019; Ujiie et al., 2018, 2019), suggest that the three shear zone exposures experienced pressures below those required for pumpellyite and glaucophane stability, as indicated in Figure 7a. This constraint suggests the Late Cretaceous plate boundary geotherm was >∼15°C/km. Calculated mineral abundances and compositions at conditions below pumpellyite-in and glaucophane-in reactions are largely dependent on T, and relatively insensitive to P (Figure 7a), precluding a more refined estimate of P.

Within the range of possible P-T paths suggested by the shear zone mineralogies within our Kyushu case study (Figure 7a), progressive subduction and increasing T between 250 and 550°C drives local phase changes that dramatically reduce the amount of mineral-bound water in a hydrated basalt composition (Figure 7b). Increasing T from within the prehnite-pumpellyite facies leads to prehnite breakdown (Figures 7 and 7c), resulting in the release of ∼5 mol% H_2O between 270°C and 290°C; close to the conditions of coastal Makimine mélange. In contrast to the coastal Makimine mélange exposures, the large area of the psuedosection occupied by the greenschist facies, and containing the peak metamorphic conditions of inland Makimine mélange exposures, experiences no substantial change to the proportion of mineral-bound water (Figure 7b). From within the greenschist facies, increasing temperature near the peak T conditions of the NMR leads to chlorite breakdown (Figures 7a and 7d), which releases another 5 mol% H_2O between 470 and 490°C. The modeled fluid release is relatively insensitive to P, and is therefore expected to occur at similar temperatures for the wide range of thermal gradients that pass through the prehnite-pumpellyite–greenschist, and greenschist–amphibolite facies transitions.

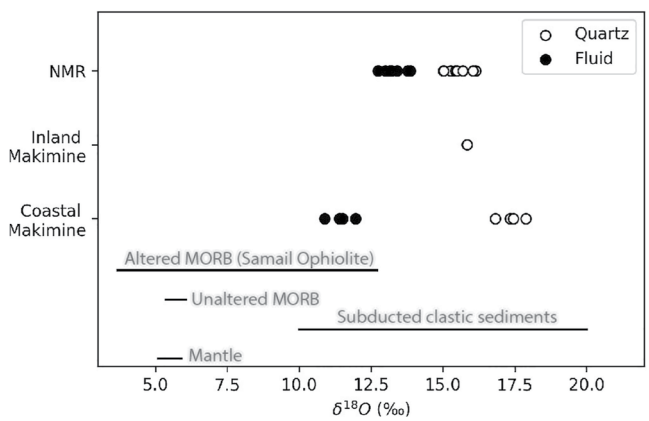

Figure 8. $\delta^{18}O$ of vein quartz for each of the localities, and for coastal Makimine mélange and the Nishisonogi metamorphic rocks (NMR), $\delta^{18}O$ of the vein-forming fluid (calculated using the Raman spectra of carbonaceous material (RSCM) estimates of peak metamorphic temperature; 371°C and 500°C, respectively). Bulk-rock $\delta^{18}O$ values were obtained from the following publications: Gregory and Taylor (1981) - altered oceanic crust; Ito et al. (1987) - unaltered basalt; Savin and Epstein (1970) - subducted clastic sediments; Mattey et al. (1994) - mantle.

4.5. $\delta^{18}O$ in Quartz Veins

Oxygen isotope ratios were measured in 4 veins within metasediment in coastal Makimine mélange, 2 veins within metasediment in inland Makimine mélange, and 8 veins within metasediment, metabasalt, and chlorite-amphibole schist from the NMR (sample descriptions and $\delta^{18}O$ values Table S2 in Supporting Information S1). Across all three shear zone exposures, $\delta^{18}O$ values in vein quartz vary between 15.0‰ and 17.9‰ (Figure 8). The highest $\delta^{18}O$ values were measured in samples from coastal Makimine mélange and lowest values measured in samples from the NMR, that is, vein $\delta^{18}O$ decreases with increasing metamorphic grade.

We calculate $\delta^{18}O$ of the vein-forming fluid for veins in the coastal Makimine mélange and in the NMR using temperature-dependent water-quartz fractionation factors (Matsuhisa et al., 1979). Veins from coastal Makimine mélange cross-cut the peak metamorphic foliation, and growth-related structures indicate formation during subduction, suggesting that the veins formed near the final stages of subduction-related deformation. Some of the veins sampled from the NMR are highly deformed and occur subparallel to the foliation, while others obliquely crosscut the foliation but also show small degrees of viscous deformation consistent with subduction, suggesting that some veins formed during the final stages of subduction-related deformation. Therefore, we use the peak metamorphic temperatures obtained by RSCM for the calculation of fluid $\delta^{18}O$ fractionation factors. Calculated fluid $\delta^{18}O$ values are 10.9‰–12.0‰ for coastal Makimine mélange veins, and 12.7‰–13.9‰ for the NMR veins (Figure 8).

5. Inferred Mechanisms of Viscous Creep Across the Base of the Subduction Thrust

5.1. Viscous Creep at <350°C

A well-developed cleavage is defined by phyllosilicates in the coastal Makimine melange (Figure 4). Intense mechanical anisotropy in phyllosilicate minerals (Hansen et al., 2020; Mares & Kronenberg, 1993; Okamoto et al., 2019) causes mechanically weak cleavage planes to be parallel to the XY plane of the finite strain ellipsoid, defined by the principal stretching directions X ≥ Y ≥ Z (Figure 9). Sigmoidal patterns of lesser and greater quartz concentration adjacent to large quartz grains (Figure 4d) are interpreted to reflect areas where relatively higher and lower normal stresses led to solubility gradients and grain elongation parallel to σ_3 (Durney, 1976; Rutter, 1983) during non-coaxial shear (Figure 9). The phyllosilicate cleavage, although formed initially perpendicular to σ_1, is expected to have rotated toward the regional shear zone boundary during progressive strain (Figure 9). In both Makimine mélange and the NMR, the lack of cleavage plane kinks within phyllosilicate grains (Figures 4f, 6b, and 6d) suggests that grain-scale frictional sliding, rather than dislocation glide, was the dominant mechanism driving deformation within phyllosilicates. Overall, the viscous fabrics in metasediments and metabasalts are interpreted to have formed during non-coaxial shear facilitated by dissolution-precipitation creep of quartz and albite, and sliding along mechanically weak chlorite and muscovite cleavages inclined to the direction of σ_1 (Fagereng et al., 2010; Niemeijer & Spiers, 2005) and subparallel to the shear zone boundary. In this case, the rheology controlling viscous shear is a frictional-viscous flow (Bos & Spiers, 2002; Niemeijer, 2018; Streit & Cox, 2000) sensitive to grain-size, mineral solubility, frictional strength, effective stress, and strain rate.

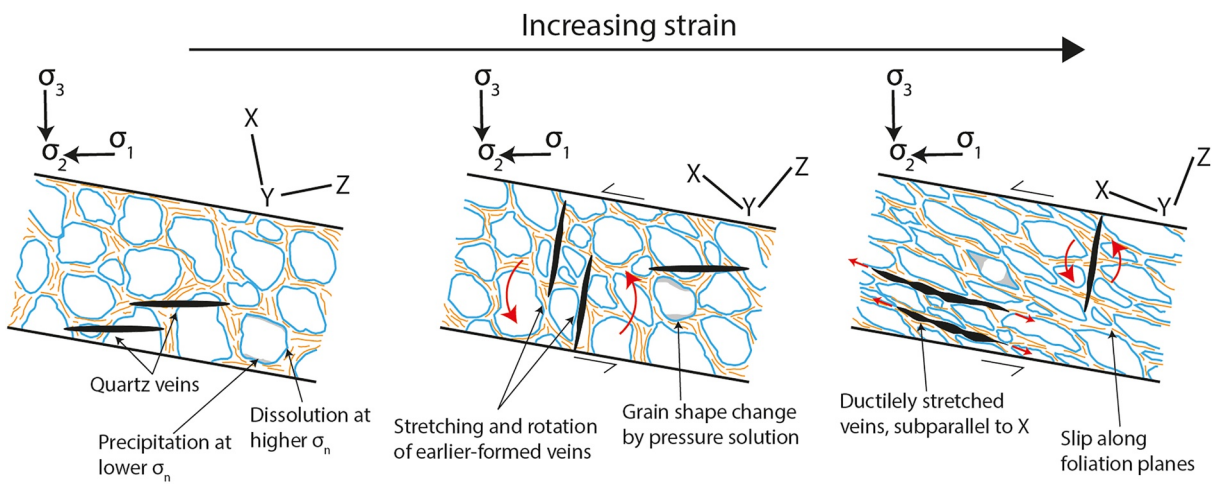

Figure 9. Development of foliation and lineation in a gently dipping simple shear zone at low angles to σ_1. Dissolution-precipitation creep of soluble minerals (blue), results in elongation of grains parallel to σ_3, assisting the formation of layers of aligned phyllosilicates (orange) along the grain boundaries of soluble minerals. Quartz veins, formed orthogonal to σ_3, will also rotate with progressive strain.

5.2. Viscous Creep at >350°C

The well-developed foliation in inland Makimine mélange is interpreted to have formed by a frictional-viscous mechanism (Figure 9) like in coastal mélange exposures. In metasediment, pronounced quartz crystal preferred orientation (CPO) patterns within relatively coarse-grained quartzite lenses, and less pronounced or absent quartz CPO patterns in adjacent mixed-mineralogy, fine-grained metasediment (Figure 5d) suggests dissolution-precipitation creep is more efficient than dislocation creep in fine grained, mixed-mineral rocks, as also inferred from theoretical (Wheeler, 1992) and laboratory (e.g., Niemeijer & Spiers, 2005) studies, and observations in some continental shear zones (e.g., Kilian et al., 2011; Stenvall et al., 2019). The sigmoidal shape of actinolite-diopside grains in metabasalt (Figure 5a) indicate that diopside breakdown occurred during non-coaxial shear.

In the NMR, viscous deformation is inferred to occur by slip along the well-developed phyllosilicate foliation (Figure 6). Well-developed shape preferred orientations and absence of CPO (Figure 6; Tulley et al., 2020) in quartz and albite suggests that these minerals deform by dissolution-precipitation creep. Therefore, like in the Makimine mélange, the bulk rheology is inferred to be controlled by a frictional-viscous flow. Boudinage of quartz veins within the inland Makimine and NMR shear zones implies that quartz is stronger than the phyllosilicate-bearing metasediments and metabasalts, highlighting the mechanical importance of phyllosilicate content.

6. Brittle Fracturing Within the Viscous Shear Zones

In coastal Makimine melange, mutually cross-cutting shear veins and extension veins formed coevally in a fault-fracture mesh (Ujiie et al., 2018). The stress and fluid pressure conditions during formation of this vein network, and the veins in the other exposures, can be explored with a brittle failure mode diagram (Cox, 2010; Sibson, 1998), plotted for Andersonian contractional and extensional stress regimes, with vertical σ_1 or σ_3, respectively (Figure 10).

The failure envelopes in Figure 10 show stress conditions for extension, extension-shear, and shear failure of isotropic rocks in effective vertical stress (σ_v') – differential stress ($\sigma_1 - \sigma_3$) space, for friction coefficients (μ) of 0.4 and 0.6, tensile strength (T_0) 5 and 10 MPa, and cohesive strengths $2T_0$. This range of material parameters is broadly representative of metasediments (e.g., Gholami & Rasouli, 2014; Lockner, 1995), and likely comparable to phyllosilicate-rich metabasalts (Figures 1c and 1d). Figure 10 also shows the stress conditions required for sliding along a cohesion-less phyllosilicate cleavage with $\mu = 0.35$, representative of experimentally deformed phyllosilicate-rich rocks (e.g., den Hartog et al., 2013; Fagereng & Ikari, 2020; Okamoto et al., 2019). Laboratory experiments indicate that the operation of dissolution-precipitation creep substantially reduces the strength of phyllosilicate-rich rocks (e.g., Niemeijer, 2018), such that the cohesionless strengths plotted in Figure 10 likely overestimate the viscous strength of the shear zone rocks. Additionally, while Figure 10 implies vein orientations are controlled by instantaneous stress orientations, the well-developed foliation in the shear zone lithologies may favor fracturing parallel to the mechanically weak foliation, at lower differential stresses than calculated in Figure 10.

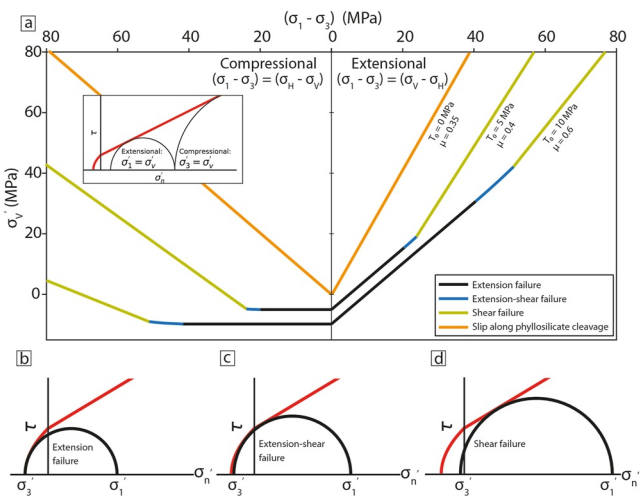

Figure 10. Stress conditions for brittle failure. (a) Failure mode diagram (after Sibson, 1998), showing extension, extension-shear, and shear failure criteria for cohesive rocks with $T_0 = 5$ and 10 MPa and $\mu = 0.6$ and 0.4. The curves plotted for $T_0 = 0$ and $\mu = 0.35$ reflect the differential stress required for slip along mechanically weak phyllosilicate cleavages. The inset Mohr diagram illustrates the effect of tectonic regime; for a given σ_v' the red curve indicating failure conditions is intersected at greater shear (τ) and effective normal stresses (σ_n') in a contractional regime. (b–d) Mohr diagrams showing stress conditions for (b) extension, (c) extension-shear, and (d) shear failure in τ-σ_n' space.

The formation of extension veins is restricted to differential stress conditions ($\sigma_1 - \sigma_3$) < $4T_0$ (Figures 10a and 10b; Etheridge, 1983; Phillips, 1974; Secor, 1965). Micaceous metasediments similar to those in coastal Makimine mélange show T_0 generally in the range 5–10 MPa (e.g., Gholami & Rasouli, 2014), suggesting differential stress conditions in coastal Makimine mélange of less than a few tens of MPa at the time of extension fracturing (Figure 10a). Shear veins in coastal Makimine mélange, formed by hybrid extensional-shear fracturing (Ujiie et al., 2018), require slightly higher differential stress (Figures 10a and 10c), but still within the order of tens of MPa. Mutually overprinting shear and extension fractures in coastal Makimine mélange imply cycling of shear stresses, perhaps reflecting transient slip

events. Subhorizontal extension veins subparallel to foliation, mutually crosscut by subvertical extension veins, imply local and/or temporary rotation of σ_3 from vertical to horizontal (Figure 10), reflecting variable shear stresses and switching between stress states favoring reverse and normal faulting, perhaps related to transient slip events (Ujiie et al., 2018). Such switching is also consistent with small differential stress, particularly if stress drops relating to fracturing and vein formation are small, as suggested by Ujiie et al. (2018). In inland Makimine mélange and the NMR, vein microstructures related to their formation (e.g., slickenfibers, euhedral grains) are overprinted by dislocation creep microstructures, making the failure mode of vein-filled fractures at these localities unclear.

Progressive viscous shear will cause rotation of veins toward parallelism with the foliation (Figure 9), suggesting that the veins in the NMR that lie oblique to foliation but are deformed with top-south shear sense must have formed during the last increment of subduction-related deformation. These observations imply that the NMR records brittle deformation that occurred at greater depths, and was superimposed on greater finite strains, than the viscous deformation recorded in inland Makimine mélange. In inland Makimine mélange, veins are viscously deformed and likely formed at shallower, cooler conditions, like those determined for coastal Makimine mélange, before being subducted deeper and deforming in a dominantly viscous part of the subduction thrust.

In the NMR, veins are more frequent near contacts between metasediment and metabasalt, relative to elsewhere in the exposures (Figures 3c–3f). In this case, local brittle failure criteria may be reached by shear stress amplification (Beall et al., 2019a; Sibson, 1980) and/or decrease in σ_3 (Cox, 2020; Fagereng, 2013) within stronger lenses, driven by faster shear strain rate in surrounding weaker rocks (Figure 11), as inferred for other lithologically heterogeneous shear zones reflecting mixed creep and fracturing (e.g., Behr & Bürgmann, 2021; Hayman & Lavier, 2014; Kotowski & Behr, 2019).

In coastal Makimine mélange and the NMR, we suggest that fracturing is caused by either, or a combination of effective stress reduction due to dehydration reactions and/or shear stress amplification due to lithological (and therefore viscosity) heterogeneity. Chemical reactions changing mineralogy along metasediment-metabasalt contacts may also assist the localisation of veining by locally releasing fluid or changing rheology (Ujiie et al., 2019). Dehydration reactions and shear stress amplification may act together to drive brittle failure within the shear zones; for example, where viscosity contrast is high, effective stresses may not need to be low to cause fracturing (e.g., Beall et al., 2019a; Fagereng & Beall, 2021). On the other hand, where the viscosity contrast is low, the degree of stress amplification is likely to be lower, and fracturing likely required lower effective stress. In coastal Makimine mélange, veins formed away from lithological contacts, perhaps reflecting fracturing dominantly driven by local fluid pressurization in the absence of stress amplification.

7. Vein Filling Volume and Fluid Sources

Along subduction *P-T* paths, the oceanic crust composition modeled in Figure 7, and other modeled subducting sediment and hydrated mantle compositions (e.g., Condit et al., 2020; Fagereng & Diener, 2011; Fagereng, Diener, Ellis, & Remitti, 2018; Hacker, 2008; Kerrick & Connolly, 2001; Peacock, 2009) release fluids at specific *P-T* conditions corresponding to dehydration reactions, with substantially lower volumes of fluid released at *P-T* conditions between these reactions. The range of potential *P-T* paths for the studied shear zones pass through two discrete *T*-dependent dehydration reactions, each releasing 5 mol% H_2O: (a) prehnite breakdown at 270–290°C and (b) chlorite breakdown at 470–490°C (Figure 7), with (a) occurring near the deformation conditions of coastal Makimine mélange and (b) occurring near the conditions of the deformation in the NMR (Figure 11a). Inland Makimine mélange preserves deformation structures that formed in a thermodynamically stable greenschist facies mineral assemblage at conditions away from ongoing dehydration reactions, and contains viscously overprinted brittle structures that potentially formed at conditions of prehnite breakdown, as preserved with much less viscous overprint in coastal Makimine mélange.

If we consider veins as formed by brittle fracture followed by fluid influx and mineral precipitation (Bons et al., 2012; Oliver & Bons, 2001), the quartz veins imply that SiO_2-saturated fluid was present within the shear zones during mixed brittle-viscous deformation. In veins from coastal Makimine mélange, variation of liquid/vapor ratios in fluid inclusions within shear veins suggest that fluid pressure cycled between near-lithostatic and near-hydrostatic values (Ujiie et al., 2018). This may be explained by fracture rapidly reducing fluid pressure, causing silica supersaturation and vein precipitation (Ujiie et al., 2018). We calculate the level of silica

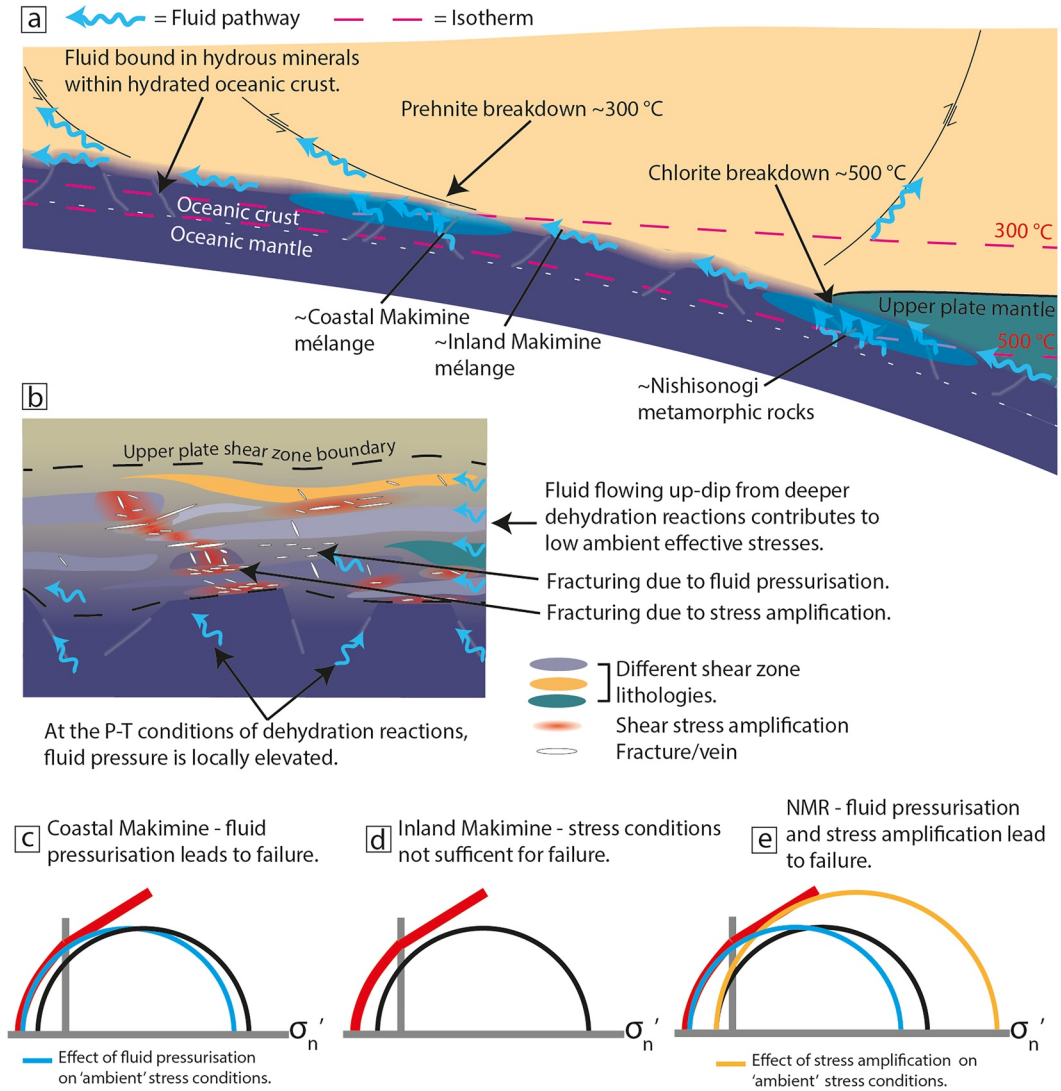

Figure 11. Summary of the effects of local dehydration reactions and lithological heterogeneity within a viscous, overpressured subduction thrust. (a) Sketch showing localized fluid inputs to an already fluid-rich thrust at the *P-T* conditions of prehnite and chlorite breakdown, lowering effective stresses and contributing to fracturing (e.g., Figures 2c and 3c). (b) Sketch of shear zone structure, based on outcrop observations (Figures 2a and 2c and Figure 3d). (c–e) Mohr circles showing "typical" states for each of the studied locations (black circles) and the effects of fluid pressurization and stress amplification.

supersaturation as the difference between the equilibrium solubility of SiO_2 in H_2O at lithostatic and hydrostatic fluid pressure, at the peak metamorphic temperature, assuming a 15°C/km thermal gradient, then calculate the volume of supersaturated fluid required to form a typical disc-shaped 1 m diameter, 3 cm thick quartz vein. Our calculations (detail in S3 of Supporting Information S1) used the equilibrium SiO_2 solubility equation of Manning (1994) and the Holland and Powell (1991) equation of state for H_2O, as implemented in MATLAB by Fagereng and Ellis (2009). Because we do not account for other sources of supersaturation, our estimates are only appropriate to demonstrate the order of magnitude of the minimum required fluid volume. To form a typical-sized vein at the conditions of coastal Makimine mélange would require at least a few hundred m^3 of fluid. In the case of the NMR, viscous overprinting has erased microstructures relating to vein formation, so we cannot constrain potential variation in fluid *P*. However, as *T* is a more important variable determining vein precipitation rate than the magnitude of fluid pressure drop (Williams & Fagereng, 2022), and assuming vein formation in the NMR occurs by a comparable process to vein formation in coastal Makimine mélange, we perform the same calculation for the NMR, which gives a minimum required fluid volume of a few tens of m^3. Although we acknowledge that the magnitude of fluid pressure drop suggested to drive precipitation is uncertain, the effect is likely less than the

order of magnitude difference we calculate between the *P-T* conditions of coastal Makimine and the NMR. As the formation of a single vein requires at least a few tens to a few hundred m^3 of fluid, and chlorite and prehnite dehydration reactions release 5 mol% H_2O from metamorphosed oceanic crust, to form a single vein from the fluid released from prehnite or chlorite dehydration would require the fluid contribution from a few hundred to a few thousand m^3 of dehydrating oceanic crust. These results suggest that the vein forming fluids are dominated by the cumulative contributions of deeper dehydration reactions, as indicated in Figure 11a.

The $\delta^{18}O$ of the vein-forming fluids may shed light on the lithologies that the fluids interacted with or were sourced from. The fluid $\delta^{18}O$ (10.9‰–13.9‰) is greater than bulk-rock $\delta^{18}O$ of unaltered oceanic crust (5.4‰–6.1‰; Ito et al., 1987) or unaltered mantle ($\delta^{18}O$ 5.1‰–5.9‰; Mattey et al., 1994). This rules out the fluids having equilibrated with these lithologies immediately prior to vein formation. However, the fluid $\delta^{18}O$ values overlap with values reported for altered oceanic crust (3.7‰–12.7‰; Gregory & Taylor, 1981) and subducted clastic sediments ($\delta^{18}O$ 10‰–20‰; Savin & Epstein, 1970). Therefore, the vein-forming fluids must have interacted with, and/or be partially or wholly sourced from, subducted sediments and altered oceanic crust. The fluid $\delta^{18}O$ values are also comparable to values for vein-forming fluids in the amphibolite facies Kuiseb Schist (11‰–13‰; Fagereng, Diener, Meneghini, et al., 2018), and vein-forming fluids in the blueschist to amphibolite-facies units of the Catalina Schist (12‰–14‰; Bebout, 1991), but slightly greater than values for vein-forming fluids in the southern Arosa Zone, Central Alps (6.7‰–10‰; Condit et al., 2022). These and our results suggest that plate boundary fluids commonly equilibrate with metasediments and altered oceanic crust (metabasalt), consistent with channeling of fluids along the plate boundary shear zone.

Considering that the metasediment mineral assemblage is nearly constant between the three localities, changes to the metasediment water content during subduction from coastal Makimine to NMR depths were likely minor. Pseudosection models of the average oceanic sediment composition GLOSS (Plank & Langmuir, 1998) support this notion, gradually releasing ~1.2 mol% H_2O along the prograde *P-T* path inferred for shear zones studied here (Fagereng, Diener, Ellis, & Remitti, 2018). In comparison, the mineralogy (Figure 7a) and water content (Figure 7b) of metabasalt changes substantially, releasing 10 mol.% water between prehnite-pumpellyite and amphibolite facies conditions. This suggests that local fluid contributions to the shear zones were dominantly sourced from metabasalts.

Measurements of noble gas ratios in veins from coastal Makimine mélange suggest that the vein-forming fluid contained 80%–85% mantle-derived fluid, 15%–18% oceanic crust-derived fluid, and the small remainder sourced from dehydrating sediments (N. Nishiyama, Sumino, & Ujiie, 2020). These results suggest that vein-forming fluids may have had $\delta^{18}O$ buffered to higher values by relatively high $\delta^{18}O$ metabasalts and metasediments, for example, by focused fluid flow along a plate boundary shear zone containing these lithologies. The modest proportion of the vein-forming fluid suggested to have an oceanic crust source (15%–18%; N. Nishiyama, Sumino, & Ujiie, 2020) suggest that local dehydration reactions in oceanic crust give a small contribution to total fluid volume within the shear zone relative to the contribution from far-field, likely deeper-derived fluids. This is consistent with our calculations that suggest local dehydration reactions produce a minor proportion of the vein-forming fluid. Far-field fluids are likely sourced from other dehydration reactions occurring at greater *P-T* conditions. For example, serpentine, which is common within hydrated ultramafic rocks, contains ~13 wt% H_2O and breaks down at >600°C along subduction *P-T* paths (Condit et al., 2020). Serpentine breakdown in subducting slab mantle and mantle wedge likely contributes substantially to the far-field derived fluid component.

These far-field sourced fluids are expected to migrate up-dip within the shear zone relatively uniformly, providing low ambient effective stresses along the plate boundary. Within a shear zone under low ambient effective stresses, local fluid contributions, such as fluid released during prehnite and chlorite breakdown, and variations in stress state along shear zone viscosity contrasts, may provide the small stress change required to locally switch between creeping behavior and localized fracturing (Figures 10 and 11).

8. Implications for Deformation Processes in Subduction Zones

8.1. Relation to Slip Styles Along Active Margins

Dissolution-precipitation creep and sliding along foliation surfaces (Figure 9) persists as the dominant mechanism within the plate boundary shear zone in metasediments and hydrated basalts over the entire range of *P-T* conditions recorded by the studied exposures. Microstructures indicating this deformation mechanism have also been observed in subduction thrust shear zones exhumed from temperatures <300°C (e.g., Meneghini & Moore, 2007;

Palazzin et al., 2016), at comparable conditions to the studied shear zones (e.g., French & Condit, 2019; Platt et al., 2018), and also at warmer conditions in continental crust (e.g., Condit & Mahan, 2018; Stenvall et al., 2019). This mechanism likely accommodates plate-rate creep at displacement rates of a few cm per year and stresses of no more than a few 10s of MPa (e.g., Wassmann & Stöckhert, 2013; Fagereng & den Hartog, 2017). At higher stresses, it may also accommodate discontinuous slow slip events at rates of a few cm per month under some conditions (e.g., Fagereng et al., 2014; Fagereng & den Hartog, 2017; Kirkpatrick et al., 2021), although other calculations have shown the required stresses to be too high (Condit et al., 2022), or that some additional weakening mechanism is required (Beall et al., 2019b).

Tectonic tremor signals are generally accepted to reflect low frequency earthquakes accommodating shear slip within the plate interface (e.g., Ide et al., 2007; Royer & Bostock, 2014; Shelly et al., 2006), although Frank et al. (2014) show that low frequency earthquakes may not encompass the entire tremor signal. Acoustic emissions during laboratory dehydration experiments are comparable to tremor (Burlini et al., 2009), and dehydration-related extension fractures perhaps reflect the noisy part of the tremor signal (Fagereng, Diener, Meneghini, et al., 2018). For shear slip events with displacement 0.1–0.2 mm along 1–10 m long faults in coastal Makimine mélange, assuming a low shear modulus (3 GPa), Ujiie et al. (2018) calculated stress drops 30–600 kPa, consistent with low driving stresses. Unfortunately, viscous overprinting has erased most, if not all, vein growth-related microstructures, preventing an estimate of stress drop for NMR veins. However, large (>1 mm) highly strained quartz grains within the veins (Tulley et al., 2020) may have formed during single episodes of vein precipitation and if so, suggest larger opening increments than for coastal Makimine mélange.

The relatively local and small-displacement fracturing recorded in coastal Makimine mélange and the NMR is indicative of a small contribution of brittle failure to a dominantly viscous regime, as for example, suggested by Gao and Wang (2017) as a mechanism for ETS below the base of the seismogenic zone. Additionally, the length-scales of vein concentration zones in coastal Makimine mélange and the NMR are on the order of tens to a few hundreds of meters, consistent with source lengths of a few hundred meters inferred for low frequency earthquakes in Cascadia (Chestler & Creager, 2017). Assuming a shear modulus 3 GPa (consistent with foliated micaceous rocks; Gholami & Rasouli, 2014), crack-seal textures with slip increments 0.1–0.2 mm within 1–10 m diameter shear veins in coastal Makimine mélange reflect episodic moment release in the order of $2 \times 10^5 - 5 \times 10^7$ Nm. These results suggest that the incremental moment release during crack-seal vein formation in coastal Makimine mélange was smaller than the moment release calculated for low frequency earthquakes associated with ETS events along the Cascadia margin ($\sim 2 \times 10^{11}$ Nm; Sweet et al., 2019). If low frequency earthquakes represent failure along multiple shear veins within a fault-fracture mesh, then this may explain the smaller moment release associated with the opening of individual shear veins.

Along the northern Hikurangi margin, the relative magnitudes of the principal compressive stresses decrease prior to SSEs and increase during SSEs, interpreted to reflect transient fluctuations in fluid pressure driving the periodicity of ETS events (Warren-Smith et al., 2019). Along the Cascadia margin, temporal changes in shear wave velocity contrast after ETS events are interpreted to reflect temporary reduction in fluid pressure after SSEs (Gosselin et al., 2020), also consistent with fluid pressure fluctuations over the ETS cycle. The cyclic fluid pressure and vein formation inferred at low effective stress conditions in the Makimine melange and NMR (Figure 11) is therefore comparable to transient conditions associated with SSEs.

8.2. Effects of Metamorphic Dehydration Reactions

Geophysical studies have shown that tremor is sensitive to small (1–15 kPa) stress changes induced by Earth and ocean tides (Nakata et al., 2008; Royer et al., 2015; Rubinstein et al., 2008; Thomas et al., 2013), indicating that stress conditions in ETS regions are close to the critical conditions for brittle failure (e.g., Figure 11). Provided that permeability is sufficiently low, pressurized fluids derived from a combination of deeper distal dehydration reactions, and local dehydration reactions, may facilitate the low effective stresses required to cause fracturing. For our Kyushu example, we infer that prehnite and chlorite dehydration locally increased the rate of fluid supply to the thrust (Figure 11), generating patches where effective stress was especially low (Figure 11a), contributing to embrittlement. In this realm, viscous deformation dominates, and brittle deformation is allowed by local failure conditions but limited in space because propagating fractures must overcome a large difference between ambient stress and frictional strength (Fagereng & Beall, 2021).

Forming the mineral equilibria calculated to occur at the *P-T* conditions of the shear zones requires the addition of water to unaltered oceanic crust, possible through sea-floor hydrothermal circulation, faulting along transforms, or along the outer-rise of subduction zones (Alt et al., 1986; Ranero et al., 2003; Shillington et al., 2015). Given that these hydration mechanisms are intrinsically local, rather than necessarily pervasive throughout the pre-subduction oceanic crust, the scale at which the equilibrium assemblages develop is likely an important control on the rheology of subducting oceanic crust. As the fluid contributions from local dehydration reactions are volumetrically small relative to the distally-derived fluid component, spatial and temporal variations in the flux of distally-derived fluid component might also cause patches of local, temporary embrittlement.

The viscous deformation recorded in the inland Makimine mélange occurred within a broad *P-T* region within the greenschist facies, where the mineral assemblage is stable and little metamorphic fluid is released (Figure 7). Subdued rates of local fluid release and low viscosity contrast suppress brittle failure, allowing viscous plate boundary rate shear by dissolution-precipitation creep and sliding along phyllosilicate foliations, provided permeability allows for efficient up-dip migration of deeper-sourced fluids. We suggest that, here, stresses are relatively stable, and sub-critical (Figure 11c).

9. Conclusions

We have considered structures that formed by creep and fracture processes within three shear zone exposures exhumed from different metamorphic grades along a kinematically similar Late Cretaceous subduction thrust. Estimates of the peak metamorphic conditions suggest the three exposures deformed within a *T* range spanning ~300°C–500°C, extending between the base of the thermally-controlled seismogenic zone and the mantle wedge corner. Metabasalts (altered oceanic crust), and subducted sediments deformed within a broad shear zone, by sliding along mechanically weak phyllosilicate foliations and dissolution-precipitation creep of interstitial non-phyllosilicates, at shear stresses sensitive to grain size, friction, mineral solubility, effective stress, and strain rate. Fracturing accompanied viscous creep at *P-T* conditions corresponding to specific metamorphic dehydration reactions in subducting oceanic crust; prehnite breakdown at 270°C–290°C and chlorite breakdown at 450°C–480°C. At these localities, effective stress is low, and only small stress perturbations are required to cause embrittlement. Shear zone rocks deformed at *P-T* conditions between these dehydration reactions deformed by viscous creep, reflected by continuous deformation structures. In heterogeneous shear zones reflect mixed creep and fracturing, the distribution of quartz veins suggests that variations in shear stress (and related strain rates) along mechanical contrasts, as well as variations in pore fluid pressure, contributed to local, transient embrittlement.

Our results imply that specific dehydration reactions can drive localized embrittlement within the viscous subduction thrust. Our results also imply that embrittlement can be driven by local variations in stresses within lithologically heterogeneous shear zones, but that this effect is more apparent if effective stresses are low or viscosity contrasts are high. Consequently, the hydration state and mineralogy of the subducting lithosphere (controlling the location and magnitude of dehydration-related fluid flux), and presence of lithological heterogeneity within the plate boundary are both potential drivers of the occurrence and distribution of brittle fracturing along otherwise viscous subduction thrusts.

Acknowledgments
This work was supported by the European Research Council (ERC) under the European Union's Horizon 2020 research and innovation program (Starting Grant agreement 715836 "MICA"), and the Japan Society for the Promotion of Science KAKENHI grants JP16H06476 and 20KK0078. Thanks to Naoki Nishiyama, Haruna Masuyama, Kazuya Noro, and Noah Phillips for their help with the fieldwork, and to Sandra Piazolo and James Lambert-Smith for their input on an earlier version. Thanks to Whitney Behr for editorial handling, and Stephen Cox and an anonymous reviewer for constructive reviews that significantly improved the manuscript.

Data Availability Statement

The raw EBSD data used to quantify quartz grain orientations, along with a description of the data analysis and cleanup routine are available from the Cardiff University Research Portal (https://doi.org/10.17035/d.2021.0137148552).

References

Alt, J. C., Honnorez, J., Laverne, C., & Emmermann, R. (1986). Hydrothermal alteration of a 1 km section through the upper oceanic crust, deep sea drilling project hole 504B: Mineralogy, chemistry and evolution of seawater-basalt interactions. *Journal of Geophysical Research*, *91*(B10), 309–335. https://doi.org/10.1029/JB091iB10p10309

Bachmann, F., Hielscher, R., & Schaeben, H. (2010). Texture analysis with MTEX - Free and open source software toolbox. *Solid State Phenomena*, *160*, 63–68. https://doi.org/10.4028/www.scientific.net/SSP.160.63

Beall, A., Fagereng, Å., & Ellis, S. (2019a). Fracture and weakening of jammed subduction shear zones, leading to the generation of slow slip events. *Geochemistry, Geophysics, Geosystems*, *20*(11), 4869–4884. https://doi.org/10.1029/2019GC008481

Beall, A., Fagereng, Å., & Ellis, S. (2019b). Strength of strained two-phase mixtures: Application to rapid creep and stress amplification in subduction zone mélange. *Geophysical Research Letters*, *46*(1), 169–178. https://doi.org/10.1029/2018GL081252

Bebout, G. E. (1991). Field-based evidence for devolatilization in subduction zones: Implications for arc magmatism. *Science*, *251*(4992), 413–416. https://doi.org/10.1126/science.251.4992.413

Behr, W. M., & Bürgmann, R. (2021). What's down there? The structures, materials and environment of deep-seated slow slip and tremor. *Philosophical Transactions of the Royal Society A: Mathematical, Physical & Engineering Sciences*, *379*(2193), 20200218. https://doi.org/10.1098/rsta.2020.0218

Bons, P. D., Elburg, M. A., & Gomez-Rivas, E. (2012). A review of the formation of tectonic veins and their microstructures. *Journal of Structural Geology*, *43*, 33–62. https://doi.org/10.1016/j.jsg.2012.07.005

Bos, B., & Spiers, C. J. (2002). Frictional-viscous flow of phyllosilicate-bearing fault rock: Microphysical model and implications for crustal strength profiles. *Journal of Geophysical Research*, *107*(B2), 1–13. https://doi.org/10.1029/2001JB000301

Brace, W. F., & Kohlstedt, D. L. (1980). Limits on lithospheric stress imposed by laboratory experiments. *Journal of Geophysical Research*, *85*(B11), 6248–6252. https://doi.org/10.1029/JB085iB11p06248

Burlini, L., Di Toro, G., & Meredith, P. (2009). Seismic tremor in subduction zones: Rock physics evidence. *Geophysical Research Letters*, *36*(8), 1–5. https://doi.org/10.1029/2009GL037735

Chestler, S. R., & Creager, K. C. (2017). A Model for low-frequency earthquake slip. *Geochemistry, Geophysics, Geosystems*, *18*(12), 4690–4708. https://doi.org/10.1002/2017GC007253

Compton, K. E., Kirkpatrick, J. D., & Holk, G. J. (2017). Cyclical shear fracture and viscous flow during transitional ductile-brittle deformation in the Saddlebag Lake Shear Zone, California. *Tectonophysics*, *708*, 1–14. https://doi.org/10.1016/j.tecto.2017.04.006

Condit, C. B., French, M. E., Hayles, J. A., Yeung, L. Y., Chin, E. J., & Lee, C.-T. A. (2022). Rheology of metasedimentary rocks at the base of the subduction seismogenic zone. *Geochemistry, Geophysics, Geosystems*, *23*(2), 1–32. https://doi.org/10.1029/2021GC010194

Condit, C. B., Guevara, V. E., Delph, J. R., & French, M. E. (2020). Slab dehydration in warm subduction zones at depths of episodic slip and tremor. *Earth and Planetary Science Letters*, *552*, 1–12. https://doi.org/10.1016/j.epsl.2020.116601

Condit, C. B., & Mahan, K. H. (2018). Fracturing, fluid flow and shear zone development: Relationships between chemical and mechanical processes in Proterozoic mafic dykes from southwestern Montana, USA. *Journal of Metamorphic Geology*, *36*(2), 195–223. https://doi.org/10.1111/jmg.12289

Cox, S. F. (2010). The application of failure mode diagrams for exploring the roles of fluid pressure and stress states in controlling styles of fracture-controlled permeability enhancement in faults and shear zones. *Geofluids*, *10*(1–2), 217–233. https://doi.org/10.1111/j.1468-8123.2010.00281.x

Cox, S. F. (2020). Chapter 2: The dynamics of permeability enhancement and fluid flow in overpressured, fracture-controlled hydrothermal systems. In *Applied structural geology of ore-forming hydrothermal systems* (pp. 25–82). Society of Economic Geologists. https://doi.org/10.5382/rev.21.02

den Hartog, S. A. M., Niemeijer, A. R., & Spiers, C. J. (2013). Friction on subduction megathrust faults: Beyond the illite-muscovite transition. *Earth and Planetary Science Letters*, *373*, 8–19. https://doi.org/10.1016/j.epsl.2013.04.036

Durney, D. W. (1976). A Discussion on natural strain and geological structure - Pressure-solution and crystallization deformation. *Philosophical Transactions of the Royal Society of London - Series A: Mathematical and Physical Sciences*, *283*(1312), 229–240. https://doi.org/10.1098/rsta.1976.0081

Etheridge, M. A. (1983). Differential stress magnitudes during regional deformation and metamorphism: Upper bound imposed by tensile fracturing. *Geology*, *11*(4), 231. https://doi.org/10.1130/0091-7613(1983)11<231:dsmdrd>2.0.co;2

Fagereng, Å. (2013). On stress and strain in a continuous-discontinuous shear zone undergoing simple shear and volume loss. *Journal of Structural Geology*, *50*, 44–53. https://doi.org/10.1016/j.jsg.2012.02.016

Fagereng, Å., & Beall, A. (2021). Is complex fault zone behaviour a reflection of rheological heterogeneity? *Philosophical Transactions of the Royal Society A: Mathematical, Physical & Engineering Sciences*, *379*(2193), 1–23. https://doi.org/10.1098/rsta.2019.0421

Fagereng, Å., & den Hartog, S. A. M. (2017). Subduction megathrust creep governed by pressure solution and frictional-viscous flow. *Nature Geoscience*, *10*(1), 51–57. https://doi.org/10.1038/ngeo2857

Fagereng, Å., & Diener, J. F. A. (2011). Non-volcanic tremor and discontinuous slab dehydration. *Geophysical Research Letters*, *38*(15), 1–5. https://doi.org/10.1029/2011GL048214

Fagereng, Å., Diener, J. F. A., Ellis, S., & Remitti, F. (2018). Fluid-related deformation processes at the up- and down-dip limits of the subduction thrust seismogenic zone: What do the rocks tell us? In *Geology and tectonics of subduction zones: A tribute to Gaku Kimura* (Vol. 534, pp. 187–215). Geological Society of America. https://doi.org/10.1130/2018.2534(12)

Fagereng, Å., Diener, J. F. A., Meneghini, F., Harris, C., & Kvadsheim, A. (2018). Quartz vein formation by local dehydration embrittlement along the deep, tremorgenic subduction thrust interface. *Geology*, *46*(1), 67–70. https://doi.org/10.1130/G39649.1

Fagereng, Å., & Ellis, S. (2009). On factors controlling the depth of interseismic coupling on the Hikurangi subduction interface, New Zealand. *Earth and Planetary Science Letters*, *278*(1–2), 120–130. https://doi.org/10.1016/j.epsl.2008.11.033

Fagereng, Å., Hillary, G. W. B., & Diener, J. F. A. (2014). Brittle-viscous deformation, slow slip, and tremor. *Geophysical Research Letters*, *41*(12), 4159–4167. https://doi.org/10.1002/2014GL060433

Fagereng, Å., & Ikari, M. J. (2020). Low-temperature frictional characteristics of chlorite-epidote-amphibole assemblages: Implications for strength and seismic style of retrograde fault zones. *Journal of Geophysical Research: Solid Earth*, *125*(4), 1–16. https://doi.org/10.1029/2020JB019487

Fagereng, Å., Remitti, F., & Sibson, R. H. (2010). Shear veins observed within anisotropic fabric at high angles to the maximum compressive stress. *Nature Geoscience*, *3*(7), 482–485. https://doi.org/10.1038/ngeo898

Faure, M., Fabbri, O., & Monie, P. (1988). The miocene bending of southwest Japan: New $^{39}Ar/^{40}Ar$ and microtectonic constraints from the Nagasaki schists (Western Kyushu), an extension of the Sanbagawa high-pressure belt. *Earth and Planetary Science Letters*, *91*(1–2), 105–116. https://doi.org/10.1016/0012-821X(88)90154-9

Fisher, D. M., Brantley, S. L., Everett, M., & Dzvonik, J. (1995). Cyclic fluid flow through a regionally extensive fracture network within the Kodiak accretionary prism. *Journal of Geophysical Research*, *100*(B7), 12881–12894. https://doi.org/10.1029/94JB02816

Frank, W. B., Shapiro, N. M., Husker, A. L., Kostoglodov, V., Romanenko, A., & Campillo, M. (2014). Using systematically characterized low-frequency earthquakes as a fault probe in Guerrero, Mexico. *Journal of Geophysical Research: Solid Earth*, *119*(10), 7686–7700. https://doi.org/10.1002/2014JB011457

French, M. E., & Condit, C. B. (2019). Slip partitioning along an idealized subduction plate boundary at deep slow slip conditions. *Earth and Planetary Science Letters*, *528*, 115828. https://doi.org/10.1016/j.epsl.2019.115828

Gao, X., & Wang, K. (2017). Rheological separation of the megathrust seismogenic zone and episodic tremor and slip. *Nature*, *543*(7645), 416–419. https://doi.org/10.1038/nature21389

Gholami, R., & Rasouli, V. (2014). Mechanical and elastic properties of transversely isotropic slate. *Rock Mechanics and Rock Engineering*, *47*(5), 1763–1773. https://doi.org/10.1007/s00603-013-0488-2

Giuntoli, F., & Viola, G. (2021). Cyclic brittle-ductile oscillations recorded in exhumed high-pressure continental units: A record of deep episodic tremor and slow slip events in the northern apennines. *Geochemistry, Geophysics, Geosystems*, *22*(9), 1–27. https://doi.org/10.1029/2021GC009805

Gosselin, J. M., Audet, P., Estève, C., McLellan, M., Mosher, S. G., & Schaeffer, A. J. (2020). Seismic evidence for megathrust fault-valve behavior during episodic tremor and slip. *Science Advances*, *6*(eaay5174), 1–6. https://doi.org/10.1126/sciadv.aay5174

Green, E. C. R., White, R. W., Diener, J. F. A., Powell, R., Holland, T. J. B., & Palin, R. M. (2016). Activity-composition relations for the calculation of partial melting equilibria in metabasic rocks. *Journal of Metamorphic Geology*, *34*(9), 845–869. https://doi.org/10.1111/jmg.12211

Gregory, R. T., & Taylor, H. P. (1981). An oxygen isotope profile in a section of Cretaceous oceanic crust, Samail Ophiolite, Oman: Evidence for $\delta^{18}O$ buffering of the oceans by deep (>5 km) seawater-hydrothermal circulation at mid-ocean ridges. *Journal of Geophysical Research*, *86*(B4), 2737–2755. https://doi.org/10.1029/JB086iB04p02737

Hacker, B. R. (2008). H_2O subduction beyond arcs. *Geochemistry, Geophysics, Geosystems*, *9*(3), 1–24. https://doi.org/10.1029/2007GC001707

Hansen, L. N., David, E. C., Brantut, N., & Wallis, D. (2020). Insight into the microphysics of antigorite deformation from spherical nanoindentation. *Philosophical Transactions of the Royal Society A: Mathematical, Physical & Engineering Sciences*, *378*(2165), 1–21. https://doi.org/10.1098/rsta.2019.0197

Hara, H., & Kimura, K. (2008). Metamorphic and cooling history of the Shimanto accretionary complex, Kyushu, Southwest Japan: Implications for the timing of out-of-sequence thrusting. *Island Arc*, *17*(4), 546–559. https://doi.org/10.1111/j.1440-1738.2008.00636.x

Harris, C., & Vogeli, J. (2010). Oxygen isotope composition of garnet in the peninsula granite Cape granite suite South Africa:constraints on melting and emplacement mechanisms. *South African Journal of Geology*, *113*(4), 401–412. https://doi.org/10.2113/gssajg.113.4.401

Hattori, H., & Shibata, K. (1982). Radiometric dating of pre-Neogene granitic and metamorphic rocks in northwest Kyushu, Japan - With emphasis on geotectonics of the Nishisonogi zone. *Bulletin of the Geological Survey of Japan*, *33*, 57–84.

Hayman, N. W., & Lavier, L. L. (2014). The geologic record of deep episodic tremor and slip. *Geology*, *42*(3), 195–198. https://doi.org/10.1130/G34990.1

Holland, T. J. B., & Powell, R. (1991). A Compensated-Redlich-Kwong (CORK) equation for volumes and fugacities of CO_2 and $H_2$2O in the range 1 bar to 50 kbar and 100-1600°C. *Contributions to Mineralogy and Petrology*, *109*(2), 265–273. https://doi.org/10.1007/BF00306484

Holland, T. J. B., & Powell, R. (2011). An improved and extended internally consistent thermodynamic dataset for phases of petrological interest, involving a new equation of state for solids. *Journal of Metamorphic Geology*, *29*(3), 333–383. https://doi.org/10.1111/j.1525-1314.2010.00923.x

Hyndman, R. D., Yamano, M., & Oleskevich, D. A. (1997). The seismogenic zone of subduction thrust faults. *Island Arc*, *6*(3), 244–260. https://doi.org/10.1111/j.1440-1738.1997.tb00175.x

Ide, S., Shelly, D. R., & Beroza, G. C. (2007). Mechanism of deep low frequency earthquakes: Further evidence that deep non-volcanic tremor is generated by shear slip on the plate interface. *Geophysical Research Letters*, *34*(3), 1–5. https://doi.org/10.1029/2006GL028890

Ito, E., White, W. M., & Göpel, C. (1987). The O, Sr, Nd and Pb isotope geochemistry of MORB. *Chemical Geology*, *62*(3–4), 157–176. https://doi.org/10.1016/0009-2541(87)90083-0

Kerrick, D. M., & Connolly, J. (2001). Metamorphic devolatilization of subducted oceanic metabasalts: Implications for seismicity, arc magmatism and volatile recycling. *Earth and Planetary Science Letters*, *189*(1–2), 19–29. https://doi.org/10.1016/S0012-821X(01)00347-8

Kilian, R., Heilbronner, R., & Stünitz, H. (2011). Quartz grain size reduction in a granitoid rock and the transition from dislocation to diffusion creep. *Journal of Structural Geology*, *33*(8), 1265–1284. https://doi.org/10.1016/j.jsg.2011.05.004

Kimura, G. (1997). Cretaceous episodic growth of the Japanese Islands. *Island Arc*, *6*(1), 52–68. https://doi.org/10.1111/j.1440-1738.1997.tb00040.x

Kirkpatrick, J. D., Fagereng, Å., & Shelly, D. R. (2021). Geological constraints on the mechanisms of slow earthquakes. *Nature Reviews Earth & Environment*, *2*(4), 285–301. https://doi.org/10.1038/s43017-021-00148-w

Kotowski, A. J., & Behr, W. M. (2019). Length scales and types of heterogeneities along the deep subduction interface: Insights from exhumed rocks on Syros Island, Greece. *Geosphere*, *15*(4), 1038–1065. https://doi.org/10.1130/GES02037.1

Leake, B. E., Woolley, A. R., Arps, C. E. S., Birch, W. D., Gilbert, M. C., Grice, J. D., et al. (1997). Nomenclature of amphiboles; Report of the subcommittee on amphiboles of the international mineralogical association commission on new minerals and mineral names. *The Canadian Mineralogist*, *35*(405), 219–246. https://doi.org/10.1180/minmag.1997.061.405.13

Liou, J. G. (1971). Analcime equilibria. *Lithos*, *4*(4), 389–402. https://doi.org/10.1016/0024-4937(71)90122-8

Lockner, D. A. (1995). Rock failure. In T. Julian Ahrens (Ed.), *Rock physics and phase relations, a handbook of physical constants* (pp. 127–147). American Geophysical Union.

Mackenzie, J. S., Needham, D. T., & Agar, S. M. (1987). Progressive deformation in an accretionary complex: An example from the Shimanto belt of eastern Kyushu, southwest Japan. *Geology*, *15*(4), 353. https://doi.org/10.1130/0091-7613(1987)15<353:PDIAAC>2.0.CO;2

Manning, C. E. (1994). The solubility of quartz in H_2O in the lower crust and upper mantle. *Geochimica et Cosmochimica Acta*, *58*(22), 4831–4839. https://doi.org/10.1016/0016-7037(94)90214-3

Mares, V., & Kronenberg, A. (1993). Experimental deformation of muscovite. *Journal of Structural Geology*, *15*(9–10), 1061–1075. https://doi.org/10.1016/0191-8141(93)90156-5

Marone, C. (1998). Laboratory-derived friction laws and their application to seismic faulting. *Annual Review of Earth and Planetary Sciences*, *26*(1), 643–696. https://doi.org/10.1146/annurev.earth.26.1.643

Matsuhisa, Y., Goldsmith, J. R., & Clayton, R. N. (1979). Oxygen isotopic fractionation in the system quartz-albite-anorthite-water. *Geochimica et Cosmochimica Acta*, *43*(7), 1131–1140. https://doi.org/10.1016/0016-7037(79)90099-1

Mattey, D., Lowry, D., & Macpherson, C. (1994). Oxygen isotope composition of mantle peridotite. *Earth and Planetary Science Letters*, *128*(3–4), 231–241. https://doi.org/10.1016/0012-821X(94)90147-3

McCrory, P. A., Hyndman, R. D., & Blair, J. L. (2014). Relationship between the Cascadia fore-arc mantle wedge, nonvolcanic tremor, and the downdip limit of seismogenic rupture. *Geochemistry, Geophysics, Geosystems*, *15*(4), 1071–1095. https://doi.org/10.1002/2013GC005144

Meneghini, F., & Moore, J. C. (2007). Deformation and hydrofracture in a subduction thrust at seismogenic depths: The Rodeo Cove thrust zone, Marin Headlands, California. *The Geological Society of America Bulletin*, *119*(1–2), 174–183. https://doi.org/10.1130/B25807.1

Miyazaki, K., Ozaki, M., Saito, M., & Toshimitsu, S. (2016). The Kyushu-Ryukyu arc. In T. Moreno, S. Wallis, T. Kojima, & W. Gibbons (Eds.), *The geology of Japan* (pp. 139–174). Geological Society London. https://doi.org/10.1144/GOJ.6

Mori, Y., Shigeno, M., Miyazaki, K., & Nishiyama, T. (2019). Peak metamorphic temperature of the Nishisonogi unit of the Nagasaki metamorphic rocks, Western Kyushu, Japan. *Journal of Mineralogical and Petrological Sciences*, *114*(4), 170–177. https://doi.org/10.2465/jmps.190423

Morimoto, N., Fabries, J., Ferguson, A. K., Ginzburg, I. V., Ross, M., Seifert, F. A., et al. (1988). Nomenclature of pyroxenes. *American Mineralogist*, *73*(367), 1123–1133. https://doi.org/10.1180/minmag.1988.052.367.15

Muller, R. D., Sdrolias, M., Gaina, C., Steinberger, B., & Heine, C. (2008). Long-term sea-level fluctuations driven by ocean basin dynamics. *Science*, *319*(5868), 1357–1362. https://doi.org/10.1126/science.1151540
Nakata, R., Suda, N., & Tsuruoka, H. (2008). Non-volcanic tremor resulting from the combined effect of Earth tides and slow slip events. *Nature Geoscience*, *1*(10), 676–678. https://doi.org/10.1038/ngeo288
Needham, D. T., & Mackenzie, J. S. (1988). Structural evolution of the Shimanto belt accretionary complex in the area of the Gokase river, Kyushu, SW Japan. *Journal of the Geological Society*, *145*(1), 85–94. https://doi.org/10.1144/gsjgs.145.1.0085
Niemeijer, A. R. (2018). Velocity-dependent slip weakening by the combined operation of pressure solution and foliation development. *Scientific Reports*, *8*(1), 4724. https://doi.org/10.1038/s41598-018-22889-3
Niemeijer, A. R., & Spiers, C. J. (2005). Influence of phyllosilicates on fault strength in the brittle-ductile transition: Insights from rock analogue experiments. *Geological Society, London, Special Publications*, *245*(1), 303–327. https://doi.org/10.1144/GSL.SP.2005.245.01.15
Nishiyama, N., Sumino, H., & Ujiie, K. (2020). Fluid overpressure in subduction plate boundary caused by mantle-derived fluids. *Earth and Planetary Science Letters*, *538*, 1–11. https://doi.org/10.1016/j.epsl.2020.116199
Nishiyama, T. (1989). Petrological study of the Nagasaki metamorphic rocks in the Nishisonogi Peninsula - With special reference to the greenstone complex and the reaction-enhanced ductility. *Memoirs of the Geological Society of Japan*, *33*, 237–257.
Nishiyama, T., Ohfuji, H., Fukuba, K., Terauchi, M., Nishi, U., Harada, K., et al. (2020). Microdiamond in a low-grade metapelite from a Cretaceous subduction complex, Western Kyushu, Japan. *Scientific Reports*, *10*(1), 1–11. https://doi.org/10.1038/s41598-020-68599-7
Obara, K. (2002). Nonvolcanic deep tremor associated with Subduction in Southwest Japan. *Science*, *296*(5573), 1679–1681. https://doi.org/10.1126/science.1070378
Obara, K., & Kato, A. (2016). Connecting slow earthquakes to huge earthquakes. *Science*, *353*(6296), 253–257. https://doi.org/10.1126/science.aaf1512
Obara, K., Tanaka, S., Maeda, T., & Matsuzawa, T. (2010). Depth-dependent activity of non-volcanic tremor in southwest Japan. *Geophysical Research Letters*, *37*(13), 1–5. https://doi.org/10.1029/2010GL043679
Okamoto, A. S., Verberne, B. A., Niemeijer, A. R., Takahashi, M., Shimizu, I., Ueda, T., & Spiers, C. J. (2019). Frictional properties of simulated chlorite gouge at hydrothermal conditions: Implications for subduction megathrusts. *Journal of Geophysical Research: Solid Earth*, *124*(5), 4545–4565. https://doi.org/10.1029/2018JB017205
Oliver, N. H. S., & Bons, P. D. (2001). Mechanisms of fluid flow and fluid-rock interaction in fossil metamorphic hydrothermal systems inferred from vein-wallrock patterns, geometry and microstructure. *Geofluids*, *1*(2), 137–162. https://doi.org/10.1046/j.1468-8123.2001.00013.x
Palazzin, G., Raimbourg, H., Famin, V., Jolivet, L., Kusaba, Y., & Yamaguchi, A. (2016). Deformation processes at the down-dip limit of the seismogenic zone: The example of Shimanto accretionary complex. *Tectonophysics*, *687*, 28–43. https://doi.org/10.1016/j.tecto.2016.08.013
Peacock, S. M. (1990). Fluid processes in subduction zones. *Science*, *248*(4953), 329–337. https://doi.org/10.1126/science.248.4953.329
Peacock, S. M. (2009). Thermal and metamorphic environment of subduction zone episodic tremor and slip. *Journal of Geophysical Research*, *114*(8), B00A07. https://doi.org/10.1029/2008JB005978
Peng, Z., & Gomberg, J. (2010). An integrated perspective of the continuum between earthquakes and slow-slip phenomena. *Nature Geoscience*, *3*(9), 599–607. https://doi.org/10.1038/ngeo940
Phillips, W. (1974). The dynamic emplacement of cone sheets. *Tectonophysics*, *24*(1–2), 69–84. https://doi.org/10.1016/0040-1951(74)90130-9
Plank, T., & Langmuir, C. H. (1998). The chemical composition of subducting sediment and its consequences for the crust and mantle. *Chemical Geology*, *145*(3–4), 325–394. https://doi.org/10.1016/S0009-2541(97)00150-2
Platt, J. P., Xia, H., & Schmidt, W. L. (2018). Rheology and stress in subduction zones around the aseismic/seismic transition. *Progress in Earth and Planetary Science*, *5*(1), 24. https://doi.org/10.1186/s40645-018-0183-8
Ranero, C. R., Phipps Morgan, J., McIntosh, K., & Reichert, C. (2003). Bending-related faulting and mantle serpentinization at the Middle America trench. *Nature*, *425*(6956), 367–373. https://doi.org/10.1038/nature01961
Rebay, G., Powell, R., & Diener, J. F. A. (2010). Calculated phase equilibria for a MORB composition in a P-T range, 450-650°C and 18-28 kbar: The stability of eclogite. *Journal of Metamorphic Geology*, *28*(6), 635–645. https://doi.org/10.1111/j.1525-1314.2010.00882.x
Rogers, G., & Dragert, H. (2003). Episodic tremor and slip on the cascadia subduction zone: The chatter of silent slip. *Science*, *300*(5627), 1942–1943. https://doi.org/10.1126/science.1084783
Rowe, C. D., Meneghini, F., & Moore, J. C. (2011). Textural record of the seismic cycle: Strain-rate variation in an ancient subduction thrust. *Geological Society, London, Special Publications*, *359*(1), 77–95. https://doi.org/10.1144/SP359.5
Royer, A. A., & Bostock, M. (2014). A comparative study of low frequency earthquake templates in northern Cascadia. *Earth and Planetary Science Letters*, *402*, 247–256. https://doi.org/10.1016/j.epsl.2013.08.040
Royer, A. A., Thomas, A. M., & Bostock, M. G. (2015). Tidal modulation and triggering of low-frequency earthquakes in northern Cascadia. *Journal of Geophysical Research: Solid Earth*, *120*(1), 384–405. https://doi.org/10.1002/2014JB011430
Rubinstein, J. L., La Rocca, M., Vidale, J. E., Creager, K. C., & Wech, A. G. (2008). Tidal modulation of nonvolcanic tremor. *Science*, *319*(5860), 186–189. https://doi.org/10.1126/science.1150558
Rutter, E. H. (1983). Pressure solution in nature, theory and experiment. *Journal of the Geological Society*, *140*(5), 725–740. https://doi.org/10.1144/gsjgs.140.5.0725
Saffer, D. M., & Tobin, H. J. (2011). Hydrogeology and mechanics of subduction zone Forearcs: Fluid flow and pore pressure. *Annual Review of Earth and Planetary Sciences*, *39*(1), 157–186. https://doi.org/10.1146/annurev-earth-040610-133408
Savin, S. M., & Epstein, S. (1970). The oxygen and hydrogen isotope geochemistry of clay minerals. *Geochimica et Cosmochimica Acta*, *34*(1), 43–63. https://doi.org/10.1016/0016-7037(70)90149-3
Scholz, C. H. (1998). Earthquakes and friction laws. *Nature*, *391*(6662), 37–42. https://doi.org/10.1038/34097
Secor, D. T. (1965). Role of fluid pressure in jointing. *American Journal of Science*, *263*(8), 633–646. https://doi.org/10.2475/ajs.263.8.633
Shelly, D. R., Beroza, G. C., Ide, S., & Nakamula, S. (2006). Low-frequency earthquakes in Shikoku, Japan, and their relationship to episodic tremor and slip. *Nature*, *442*(7099), 188–191. https://doi.org/10.1038/nature04931
Shillington, D. J., Bécel, A., Nedimović, M. R., Kuehn, H., Webb, S. C., Abers, G. A., et al. (2015). Link between plate fabric, hydration and subduction zone seismicity in Alaska. *Nature Geoscience*, *8*(12), 961–964. https://doi.org/10.1038/ngeo2586
Sibson, R. H. (1980). Transient discontinuities in ductile shear zones. *Journal of Structural Geology*, *2*(1–2), 165–171. https://doi.org/10.1016/0191-8141(80)90047-4
Sibson, R. H. (1996). Structural permeability of fluid-driven fault-fracture meshes. *Journal of Structural Geology*, *18*(8), 1031–1042. https://doi.org/10.1016/0191-8141(96)00032-6
Sibson, R. H. (1998). Brittle failure mode plots for compressional and extensional tectonic regimes. *Journal of Structural Geology*, *20*(5), 655–660. https://doi.org/10.1016/S0191-8141(98)00116-3

Sibson, R. H. (2017). Tensile overpressure compartments on low-angle thrust faults. *Earth Planets and Space*, *69*(1), 113. https://doi.org/10.1186/s40623-017-0699-y

Stenvall, C. A., Fagereng, Å., & Diener, J. F. A. (2019). Weaker than weakest: On the strength of shear zones. *Geophysical Research Letters*, *46*(13), 7404–7413. https://doi.org/10.1029/2019GL083388

Streit, J. E., & Cox, S. F. (2000). Asperity interactions during creep of simulated faults at hydrothermal conditions. *Geology*, *28*(3), 231–234. https://doi.org/10.1130/0091-7613(2000)28<231:AIDCOS>2.0.CO;2

Sweet, J. R., Creager, K. C., Houston, H., & Chestler, S. R. (2019). Variations in cascadia low-frequency earthquake behavior with downdip distance. *Geochemistry, Geophysics, Geosystems*, *20*(2), 1202–1217. https://doi.org/10.1029/2018GC007998

Taira, A., Okada, H., Whitaker, J. H., & Smith, A. J. (1982). The Shimanto belt of Japan: Cretaceous-lower Miocene active-margin sedimentation. *Geological Society, London, Special Publications*, *10*(1), 5–26. https://doi.org/10.1144/GSL.SP.1982.010.01.01

Thomas, T. W., Vidale, J. E., Houston, H., Creager, K. C., Sweet, J. R., & Ghosh, A. (2013). Evidence for tidal triggering of high-amplitude rapid tremor reversals and tremor streaks in northern Cascadia. *Geophysical Research Letters*, *40*(16), 4254–4259. https://doi.org/10.1002/grl.50832

Tulley, C. J., Fagereng, Å., & Ujiie, K. (2020). Hydrous oceanic crust hosts megathrust creep at low shear stresses. *Science Advances*, *6*(22), 1–9. https://doi.org/10.1126/sciadv.aba1529

Ujiie, K., Noro, K., Norio, S., Fagereng, Å., Nishiyama, N., Tulley, C. J., et al. (2019). Geological and rheological conditions of subduction plate boundary between the seismogenic zone and the ETS zone in warm-slab environments. In *Japan geoscience union meeting 2019*. [Conference presentation abstract].

Ujiie, K., Saishu, H., Fagereng, Å., Nishiyama, N., Otsubo, M., Masuyama, H., & Kagi, H. (2018). An explanation of episodic tremor and slow slip constrained by crack-seal veins and viscous shear in subduction mélange. *Geophysical Research Letters*, *45*(11), 5371–5379. https://doi.org/10.1029/2018GL078374

Wallis, S. R., Yamaoka, K., Mori, H., Ishiwatari, A., Miyazaki, K., & Ueda, H. (2020). The basement geology of Japan from A to Z. *Island Arc*, *29*(1), 1–31. https://doi.org/10.1111/iar.12339

Warren-Smith, E., Fry, B., Wallace, L. M., Chon, E., Henrys, S., Sheehan, A., et al. (2019). Episodic stress and fluid pressure cycling in subducting oceanic crust during slow slip. *Nature Geoscience*, *12*(6), 475–481. https://doi.org/10.1038/s41561-019-0367-x

Wassmann, S., & Stöckhert, B. (2013). Rheology of the plate interface - Dissolution precipitation creep in high pressure metamorphic rocks. *Tectonophysics*, *608*, 1–29. https://doi.org/10.1016/j.tecto.2013.09.030

Wech, A. G., & Creager, K. C. (2011). A continuum of stress, strength and slip in the Cascadia subduction zone. *Nature Geoscience*, *4*(9), 624–628. https://doi.org/10.1038/ngeo1215

Wheeler, J. (1992). Importance of pressure solution and coble creep in the deformation of polymineralic rocks. *Journal of Geophysical Research*, *97*(B4), 4579–4586. https://doi.org/10.1029/91JB02476

Whittaker, J. M., Muller, R. D., Leitchenkov, G., Stagg, H., Sdrolias, M., Gaina, C., & Goncharov, A. (2007). Major Australian-Antarctic plate reorganization at Hawaiian-emperor bend time. *Science*, *318*(5847), 83–86. https://doi.org/10.1126/science.1143769

Williams, R. T., & Fagereng, Å. (2022). The role of quartz cementation in the seismic cycle: A critical review. *Reviews of Geophysics*, *60*(1), e2021RG000768. https://doi.org/10.1029/2021RG000768

Yardley, B. W. D. (1983). Quartz veins and devolatilization during metamorphism. *Journal of the Geological Society*, *140*(4), 657–663. https://doi.org/10.1144/gsjgs.140.4.0657